Two-dimensional condensates of HRS drive the assembly of flat clathrin lattices on endosomes

Markku Hakala[1], Satish Babu Moparthi[2], Iva Ganeva[3], César Bernat-Silvestre[1], Javier Espadas[1], Wanda Kukulski[3], Stéphane Vassilopoulos[2], Marko Kaksonen[1], Aurélien Roux[1]

[1] Department of Biochemistry, University of Geneva, CH-1211 Geneva, Switzerland
[2] Sorbonne Université, INSERM, Institute of Myology, Centre of Research in Myology, UMRS 974, Paris, France.
[3] Institute of Biochemistry and Molecular Medicine, University of Bern, 3012 Bern, Switzerland

Correspondence to Aurelien.Roux@unige.ch, and Marko.Kaksonen@unige.ch.

Abstract

Amongst the different clathrin structures in mammalian cells, bi-layered clathrin coat colocalizing with endosomal sorting complex required for transport (ESCRT)-0 remains one of the most ambiguous. Despite being observed for the first time twenty years ago, their structure and how they are assembled remains unknown. Here, we reconstituted *in vitro* the ESCRT-0 clathrin assembly onto various types of membranes. The ESCRT-0 protein HRS, a known clathrin adaptor on endosomes, was found to form protein condensates. These condensates spread into a thin layer on PI(3)P-rich membranes. Platinum replica electron microscopy revealed that, surprisingly, the assembly of clathrin was different depending on the HRS phase. Protein droplets recruited clathrin as a dense, curved lattice, with many cage-like structures. On two-dimensional condensates, HRS recruited clathrin as a dense flat assembly. Two-dimensional HRS-clathrin condensates promoted the clustering of cholesterol in the underlying membrane, while cholesterol enhanced PI(3)P-dependent HRS recruitment on the membrane. On free-standing membranes, two-dimensional HRS-clathrin condensates promoted membrane flattening. Overall, these results show that a two-dimensional HRS condensate creates a unique membrane structure for sorting cargo molecules, defining a new mechanism in membrane trafficking processes.

Introduction

Clathrin, the main and first characterized component involved in clathrin-mediated endocytosis (CME), self-assembles in vitro into spherical cages that resemble the coats visualized on endocytic vesicles (Ybe et al., 1999; Liu et al., 1995). During CME, clathrin, together with membrane binding-adaptor proteins, initially assembles into a flat polygonal lattice, and through structural changes driving its assembly into hexagons and pentagons, promotes membrane deformation and invagination (Kaksonen and Roux, 2018; Sochacki and Taraska, 2019). In intracellular vesicle trafficking routes, clathrin is involved in the recycling of cargoes to the plasma membrane from recycling endosomes and export from the trans-Golgi network. During these trafficking processes, the clathrin coat assembles on the organellar membrane and facilitates membrane budding in a similar way to CME (Vassilopoulos and Montagnac, 2024).

In addition to clathrin structures that promote membrane deformation, mammalian cells have flat and tubular clathrin structures, that are usually not linked to vesicle trafficking (Vassilopoulos and Montagnac, 2024). At the plasma membrane, hexagonal clathrin lattices participate in the

formation of integrin-dependent adhesion plaques or collagen-pinching tubular adhesions (Lock et al., 2019; Hakanpää et al., 2023; Elkhatib et al., 2017). Among the flat clathrin lattices, the least understood are found on the endosomes. There, clathrin associates with the endosomal sorting complex required for transport (ESCRT)-0 complex by colocalizing with Hepatocyte growth factor tyrosine kinase substrate HRS/HGS (from now on, HRS)(Raiborg, 2001). HRS-positive clathrin domains sort ubiquitylated cargoes and and have a role in ILV formation (Raiborg et al., 2002; Wenzel et al., 2018; Migliano et al., 2023; Raiborg and Stenmark, 2009; Vietri et al., 2020). Remarkably, HRS-clathrin structures have a distinctive bi-layered organization (Sachse et al., 2002), which is unique among clathrin structures in the cell (Kukulski et al., 2012; Avinoam et al., 2015; Vassilopoulos and Montagnac, 2024). However, these ESCRT-0-positive clathrin lattices on endosomes have remained an enigma in the field ever since they were first observed under the electron microscope (Raiborg, 2001; Sachse et al., 2002).

Because clathrin itself does not bind directly to the membrane, the assembly of different clathrin structures onto different cellular membranes is mediated by the interaction of organelle-specific adaptors. HRS is a clathrin adaptor specific to the endosomes. It is recruited through interaction between its FYVE domain and phosphatidyl-inositol 3-phosphate (PI(3)P), which is enriched in early endosomal membranes and intraluminal vesicles (Gillooly, 2000; Raiborg et al., 2001; Urbé et al., 2000). Another common lipid enriched in all clathrin-binding membranes is cholesterol. Cholesterol is one of the defining factors for membrane territories, which include the Trans-Golgi network, endosomes, and the plasma membrane (Kim and Burd, 2023; Bigay and Antonny, 2012). Notably, clathrin-mediated membrane trafficking locates to these organelles. Due to its role in lateral phase separation of lipids and alteration of membrane biophysical properties, cholesterol has been involved in a plethora of membrane functions. Besides the early hypothesis that it promotes lipid raft formation for sorting proteins for vesicular trafficking, cholesterol also promotes membrane bending during CME (Anderson et al., 2021; Rodal et al., 1999; Pichler and Riezman, 2004). Cholesterol is highly enriched at multivesicular endosomes (Van Meer et al., 2008; Ikonen, 2018). While the excess of cholesterol in endosomes is well described to alter transport functions, notably in the Niemann-Pick Syndrome mutants NPC1 and NPC2, and therefore its distribution and trafficking in cells is tightly regulated (Wheeler and Sillence, 2020; Ikonen and Zhou, 2021), the physiological roles of cholesterol at endosomes remain fairly uncharacterized. Furthermore, while both are enriched in the same membrane compartments, the role of cholesterol in clathrin assembly has not been investigated extensively.

Here, we studied the assembly of ESCRT-0-positive clathrin coats on endosomes and their interplay with the underlying membrane. Our reconstitution approach revealed that HRS is recruited onto the membrane through interaction with PI(3)P, but its assembly is dramatically increased, surprisingly, by cholesterol. HRS, which contains unstructured domains, forms phase separated condensates in solution and two-dimensional condensates on membranes. While 3D protein droplets promote the assembly of spherical clathrin lattices *in vitro*, the two-dimensional condensates promote the assembly of a solid and dense, flat layer of clathrin. On liposomes, the two-dimensional condensate promotes the formation of flat clathrin domains. By studying the ultrastructure of the HRS-containing clathrin domain in the cell, we show that the extent of their recruitment to endosomes depends on cholesterol amounts and that their assembly is associated with the formation of multilayered protein coats on endosomes.

Results

HRS recruits clathrin on membranes as flat lattices and domes

To understand properties and their assembly mechanism, we initially aimed at reconstituting flat ESCRT-0 -positive clathrin lattices *in vitro*. We purified human HRS and bovine clathrin, labeled them with AlexaFluor-conjugated C_5 maleimide, and tested their binding to model membranes. As expected, HRS gets recruited onto a giant unilamellar vesicle (GUV) membranes that contain 1% PI(3)P and DOPS (Lipid mix 1, Supplementary table 2). Notably, we did not observe recruitment of HRS on GUVs containing 20% DOPS but no PI(3)P (Lipid mix 2, Supplementary table 2), indicating that HRS recruitment is facilitated through specific interaction between PI(3)P and not through electrostatics between the protein and charged lipids (Supplementary figure 1a). Following the same pattern, HRS recruits clathrin on PI(3)P-rich GUVs, and we did not observe clathrin recruitment on GUVs without PI(3)P (Supplementary figure 1b). PI(3)P is thus required for the successful reconstitution of HRS-clathrin lattices.

We next tested the recruitment kinetics of HRS on PI(3)P-rich membrane. To this end, we prepared supported lipid bilayers (SLBs) with 1% PI(3)P (Lipid mix 1, Supplementary table 2) and followed the recruitment of AlexaFluor-488 labeled HRS. Recruitment of 500 nM labeled HRS follows a pattern of a one-phase association model and plateau after 30 min (Supplementary figure 1c). To test if recruited HRS on SLBs undergo lateral diffusion, we photo-bleached a small region and followed its recovery over time. We observed a very slow recovery rate, which is an indication that there is no significant lateral diffusion of protein on the membrane (Supplementary figure 1d). These experiments reveal that HRS is readily recruited on SLBs and forms a very static protein lattice on the membrane.

We then utilized SLBs to study the dynamics of clathrin recruitment on PI(3)P-rich membrane (Lipid mix 1, Supplementary table 2). To avoid unwanted assembly of clathrin cages in solution, all experiments were performed at physiological pH and salt concentrations. Moreover, we minimized the in-solution interaction of HRS and clathrin by introducing proteins onto SLBs in a sequential manner using microfluidic chambers that were washed five times with reaction buffer after 60 min of HRS incubation and before clathrin addition (Figure 1a). Finally, the recruitment of 200 nM clathrin was measured by using fluorescently labeled protein (Figure 1b). Our experiments revealed that HRS recruits clathrin on SLBs in a concentration-dependent manner (Figure 1c-e). Both the nucleation rate and the final clathrin amount on the membrane were proportional to the HRS bulk concentration (Figure 1d-e). Clathrin recruitment followed the exponential one-phase association kinetics. Interestingly, with higher HRS concentrations, the clathrin recruitment did not seem to saturate. This could indicate that with a high concentration of HRS, a very dense clathrin lattice is assembled. We thus wanted to visualize HRS-clathrin lattices at higher resolution.

Platinum replica electron microscopy (PREM) is a powerful approach to reveal protein lattices, including clathrin patches, on flat surfaces because it provides very high contrast and allows *en face* views making it ideally suited to visualize flat polygonal lattices (Heuser, 1980; Wernert et al., 2024). We developed a technique to directly deposit SLBs on glass substrate and compared clathrin recruitment kinetics to the resulting lattice morphology. We fixed samples incubated for 60 minutes with two different concentrations of HRS and 30 minutes with a constant 200 nM concentration of clathrin with a mixture of formaldehyde and glutaraldehyde and then prepared platinum replicas of these samples for electron microscopy analysis. With 100 nM HRS, we

observed small clathrin patches on SLBs (Figure 1f). In addition, these patches were often accompanied by spherical clathrin cages. Because these cages were always connected to a neighboring clathrin patch and we never observed a cage without this link, we reasoned that they originated from initially flat clathrin lattices or were assembled as cages next to flat protein patches (Figure 1f). With 500 nM HRS and 200 nM clathrin, we frequently observed large, dense clathrin islands, which were often round-shaped (Figure 1g). These patches contained dense, flat lattices, especially in the inner region of the patch, and electron tomography revealed they are slightly higher compared to the surrounding clathrin lattice (Supplementary movie 1). The flat, dense part appeared to have relatively unstructured assemblies of clathrin, while domes exhibited the classic hexagon/pentagon lattice of clathrin cages (Figure 1g, zoom-in 2). This surprising observation suggested that clathrin does not assemble as an even lattice with HRS on SLB, but there could be different populations of clathrin lattices with HRS, possibly driven by different populations of HRS itself. It is thus possible that these populations could also depend on the kinetics of the assembly.

Taken together, our *in vitro* experiments show that HRS recruits clathrin as a flat lattice, and depending on the concentration of HRS, the lattice density varies. This lattice either remains flat or curves into domes, providing evidence that HRS-driven clathrin assembly has structural flexibility, which might depend either on HRS concentration or other biochemical or biophysical parameters. We ought to better understand which HRS parameters are important to control HRS-mediated clathrin assembly on membranes.

HRS condensates wet the supported lipid bilayer membranes

At low protein concentrations, HRS is recruited to SLBs homogenously. However, when we diluted labeled HRS protein to 2 μM in physiological salt conditions, we surprisingly observed the formation of spherical protein condensates in solution (Supplementary figure 1a). These spheres could grow by fusion and coalescence, suggesting their liquid nature (Supplementary movie 2), a defining characteristic of phase-separated protein condensates (Banani et al., 2017). Protein condensation is often driven by intrinsically disordered regions (IDRs) in proteins (Brangwynne et al., 2015). In HRS, the VHS and FYVE domains, as well as the double ubiquitin-binding motif (DUIM) at its amino terminal part and the long helix in the middle of the protein, are well structured (Supplementary figure 2b). In addition to these structured parts, according to UIPred3 prediction, HRS contains two IDRs: one between the DUIM motif and the helical region and the other one at its carboxy terminus (Supplementary figure 2b).

We wondered how these protein condensates would interact with the membrane. To test this, we introduced 2 μM labeled HRS on SLBs containing 1% PI(3)P (Lipid mix 1, Supplementary table 2). Fascinatingly, protein condensates interacted with the membrane and started spreading on it, covering the whole membrane area with a high-density protein coat (Figure 2a). When condensates landed on the membrane, protein droplets dispersed and concurrently spread on the SLB (Figure 2b) (Supplementary movie 3), further indicating that HRS condensates behave as liquid-like droplets. Interestingly, the HRS layer that spreads onto the membrane forms a two-dimensional film of apparent homogeneous thickness. This suggests that the surface interaction energy between HRS condensates and the membrane overcomes the surface tension between the condensate and the solution. To test if HRS condensates on the membrane undergo lateral protein diffusion, we photobleached small regions of the droplet-like protein condensates that had landed on the membrane, as well as on the two-dimensional protein condensate film spreading on the membrane (Supplementary figure 2c-d). Similar to the low-density, homogenous HRS population on the membrane (Supplementary figure 1d), neither of these HRS condensate populations showed a

fluorescence recovery at the photobleached region (Supplementary figure 2c-d). This indicates that when these condensates are spreading on the membrane, they are either very viscous, which would lead to negligible lateral protein diffusion, or they are interacting with the membrane, forming a higher-order protein mesh.

These observations show that HRS forms condensates in solution and completely wet the membrane. Liquid condensates of multiple proteins, such as epidermal growth factor receptor substrate 15 (Eps15), growth factor receptor-bound 2 (Grb2), and glycinin, interact with the membranes (Day et al., 2021; Mangiarotti et al., 2023b; Wang et al., 2023). However, these proteins seem to maintain their droplet-like appearance and often deform the membrane. HRS droplets readily dispersed upon interaction with the membrane, favoring full membrane wetting instead of the formation of stable protein droplets on the membrane, resembling the two-dimensional condensates reported in previous studies (Lee et al., 2019; Huang et al., 2016; Banjade and Rosen, 2014). High-energy interactions with membranes are known to favor complete membrane wetting by protein condensates (Zhao et al., 2021). Thus, the strong interaction between HRS and lipids in the SLBs could promote this wetting behavior. We demonstrated this by testing if protein condensates spread on a membrane composed of DOPC lipids only (uncharged membrane, Lipid mix 7, Supplementary table 2) or a membrane containing charged DOPS (negatively charged) as well as PI(3)P (Lipid mix 1, Supplementary table 2). HRS condensates did not adhere and spread on the DOPC-only membrane but readily spread on the DOPS/PI(3)P-rich membrane, forming a dense protein film (Supplementary figure 2e-f).

Thus, we show that HRS is recruited on the membrane through interaction with PI(3)P either as a stable and homogenous protein lattice or as a two-dimensional condensate. The formation of two-dimensional condensates is dependent on the interaction between HRS and membrane lipids. High local concentration, such as liquid-like droplets, of HRS on the membrane promotes the two-dimensional condensate formation.

Clathrin assembles as a dense lattice onto the two-dimensional HRS condensate

We wondered whether HRS condensates could recruit clathrin and how the lattice looks compared to the homogenous HRS on the membrane. To this end, we incubated PI3P-rich SLBs (Lipid mix 1, Supplementary table 2) with 2 μM HRS, and after observing droplet-like condensates forming, washed the remaining HRS out five times with reaction buffer and introduced 200 nM clathrin. Membrane-associated, droplet-like HRS condensates readily recruited clathrin, indicating that HRS remains active when forming liquid-like assemblies (Supplementary figure 3a). Notably, clathrin did not enter inside the HRS condensates but covered the surface of the protein condensate (Supplementary figure 3a). We then compared HRS and clathrin fluorescence intensities on HRS condensates and outside these regions in conditions where HRS does not wet the surface outside the droplets but binds directly to the membrane. HRS intensity is around 20 times higher inside the protein condensate region compared to the region outside the condensates (Supplementary figure 3b).

We then incubated PI(3)P-rich SLBs (Lipid mix 1, Supplementary table 2) with 2 μM HRS until the formation of two-dimensional condensates was observed. Fluorescent clathrin was again recruited onto remaining HRS droplets but also onto two-dimensional condensates (Figure 2c). We measured the fluorescence intensity of HRS and clathrin along the line drawn from the low-

density HRS region on SLB across the two-dimensional condensate towards the remaining HRS droplet. As expected, HRS fluorescence intensity increased stepwise from the low-density region to high-density two-dimensional condensate and dramatically increased at the droplet-like condensate (Figure 2d). Clathrin fluorescence intensity followed the same trend and increased at the border of two-dimensional HRS condensates and substantially increased at the HRS droplet (Figure 2d). This analysis supports the idea of three different HRS populations on the membrane: 1) low-density HRS, 2) two-dimensional HRS condensates, and 3) droplet-like HRS condensates. All populations readily recruit clathrin in an HRS-concentration dependent manner (Figure 2e).

To compare clathrin coat structures on droplets and two-dimensional condensates, we again took advantage of PREM. Platinum replica samples prepared with 2 μM HRS and 200 nM clathrin at room temperature showed extensive amounts of clathrin cages at the surface of HRS droplets (Supplementary figure 2c-e). Like fluorescence microscopy data, the clathrin cages at the surface of two-dimensional condensates next to the droplet condensates appeared flatter and less numerous than on droplets (Figure 2f, Supplementary figure 2e). Furthermore, we observed areas where flat clathrin lattices were visible (Figure 2f, Supplementary figure 2e, right panel). These flat clathrin lattices were not dissimilar to those we observed with lower HRS concentration (Figure 1g), and do not show clear hexagonal pattern but have unorganized appearance (Figure 2f, zoom-in images). We reasoned that the dynamics of spherical budding on the two different surfaces may be very different, and lead to many spherical cages on droplets with only partial cages and flat lattices on two-dimensional condensates. A previous studies with epsin and clathrin showed that clathrin coat structure depended on temperature and that at lower temperatures, they remained flat (Dannhauser and Ungewickell, 2012). We therefore tested if temperature influences clathrin assembly on HRS condensates. Remarkably, when clathrin was incubated at 4°C, it assembled on two-dimensional HRS condensates as dense, flat lattices (Figure 2g).

Taken together, our experiments revealed that the two types of HRS condensates, two-dimensional and droplet-like condensates, both can assemble a very dense clathrin lattice. Unlike HRS droplets, which promote rapid assembly into hexagonal and pentagonal spherical cages, two-dimensional condensates promoted – at least transiently – the formation of a dense, flat lattice of polymerized clathrin. These clathrin lattices show intriguing unorganized appearance without a clear hexagonal pattern often observed with flat clathrin lattices (Redlingshöfer et al., 2020; Dannhauser and Ungewickell, 2012; Dannhauser et al., 2015).

Liquid-liquid phase separation through IDRs is a phenomenon that has recently been shown to play an important role in membrane remodeling and membrane repair (Ravindran and Michnick, 2024; Yuan et al., 2021; Mangiarotti et al., 2023a; Bussi et al., 2023). In clathrin-mediated endocytosis, Eps15 and its budding yeast homolog Ede1, as well as Sla1 in budding yeast, were shown to undergo liquid condensation (Kozak and Kaksonen, 2022; Day et al., 2021; Bergeron-Sandoval et al., 2021; Wilfling et al., 2023). However, to our best knowledge, HRS is the first protein directly interacting with clathrin that undergoes condensation. Moreover, we did not find reports showing the assembly of clathrin directly on the protein condensate. Thus, HRS and clathrin are unique in combining a liquid-like protein condensate and a well-structured protein lattice in the same protein assembly.

Cholesterol enhances HRS* and clathrin *recruitment on the membrane

HRS recruitment to membranes is facilitated by the interaction between its FYVE domain and PI(3)P (Raiborg et al., 2001) (Supplementary figure 1a), and positively charged lipids enhance the membrane wetting by HRS condensates (Supplementary figure 2e-f). We next decided to investigate the contribution of cholesterol, which is prominent at endosomes and other clathrin-specific organelles (Van Meer et al., 2008; Kim and Burd, 2023; Bigay and Antonny, 2012). Cholesterol was shown to promote lipid segregation, thereby facilitating the phosphatidylinositol 4,5-biphosphate-dependent recruitment of fibroblast growth factor 2 (FGF2) and pleckstrin homology (PH) domain (Lolicato et al., 2022). We tested the recruitment of HRS on GUVs with 1% PI(3)P and varying cholesterol concentrations: 0%, 15%, and 30% cholesterol (Lipid mixes 3, 1, and 4, respectively, Supplementary table 2). To our surprise, cholesterol enhanced the recruitment of HRS on membranes (Figure 3a,c). Correspondingly, more clathrin was recruited on HRS-positive GUVs containing increasing amounts of cholesterol (Figure 3b,d). Interestingly, with 0% and 15% cholesterol, HRS was recruited on the membrane as small patches, whereas on membranes with 30% cholesterol, HRS either formed larger patches or covered the whole GUV membrane. Since HRS does not contain cholesterol-binding domains or motifs, this result suggests that cholesterol enhances HRS recruitment via an indirect mechanism, possibly through its action on promoting lipid phase separation (Wang et al., 2023; Snead and Gladfelter, 2019).

We then wanted to test if cholesterol enhances the recruitment of HRS on endosomes in cells. To this end, we used a known inhibitor of cholesterol transporter NPC1, U18666A, which elevates cholesterol in endosomal compartments (Palmulli et al., 2024; Liscum and Faust, 1989). We performed immunofluorescence staining of endogenous HRS with either HeLa MZ control cells or U18666A-treated cells. Remarkably, cells treated with the drug showed a dramatic increase in HRS fluorescence intensity compared to control cells (Figure 3e-f), indicating that more HRS is bound on endosomes in drug-treated cells. We also tested if methyl-beta-cyclodextrin (MβCD), which is well-known to remove sterols from cellular membranes (Kilsdonk et al., 1995), affects HRS localization in cells. MβCD decreased the HRS fluorescence intensity on endosomes, showing that a reduced cholesterol levels causes a detachment of HRS from cell membranes (Figure 3e,g). To confirm that HRS is still localized to endosomes upon U18666A treatment, we analyzed the colocalization of endogenous HRS with EEA1, LAMP1, and LBPA, well-known markers for endosomes and lysosomes. HRS colocalized similarly with EEA1 in control cells compared to U18666A-treated cells. In contrast, no colocalization was observed with LAMP1 and LBPA in either control or U18666A-treated cells (Supplementary figure 4a). We also analyzed the HRS localization in cells transfected with GFP-Rab5 Q79L, which enlarges endosomes and thus makes the detection of HRS localization easier, in cells treated with U18666A. HRS colocalized with GFP-Rab5 Q79L but not with LAMP1 in these cells (Supplementary figure 4b). These observations indicate that the increased HRS localization occurs mostly in the endosome population, and there is no mis-localization of HRS to lysosomes upon U18666A-induced cholesterol accumulation.

Since HRS forms distinct domains on endosomes (Raiborg et al., 2002), we decided to test if these HRS domains are rich in cholesterol. To this end, we tagged endogenous HRS in HeLa MZ cells with bright Scarlet-i3 fluorescent protein from the amino terminus of HRS using CRISPR-Cas9 (Supplementary Figure 5a). Western blot analysis revealed that one of the cell lines was heterozygous with one HRS alleles tagged, while the second cell line had both alleles tagged with Scarlet-i3. We note that tagging of HRS decreased its expression levels (Supplementary Figure 5b), and therefore we used heterozygous cell line, which has HRS expression closer to normal level than the homozygous Scarlet-I3-HRS line, in all our experiments. To confirm the correct localization of Scarlet-i3-HRS, we labeled endosomes and lysosomes with a pulse of AlexaFluor-

647 labeled epidermal growth factor (AF647-EGF), which is commonly used to detect different compartments of intracellular vesicle trafficking (Wenzel et al., 2018). Scarlet-i3-HRS colocalized with AF647-EGF after 15 minutes of AF647-EGF incubation, indicating that Scarlet-i3-tagged HRS localizes to endosomes (Supplementary figure 5c-d). These results confirmed that the tagging did not affect the localization of the protein in our cell line. We then stained cholesterol in these cells with Filipin and observed a clear colocalization of Scarlet-i3-HRS and Filipin. These data indicate that HRS domains on endosomes are indeed enriched in cholesterol and support our *in vitro* observations (Figure 3h).

Our data demonstrates that cholesterol enhances the binding of HRS on membranes both *in vitro* and in cells. We wondered if this role could be due to membrane wetting promotion by HRS. To test this, we prepared SLBs with varying cholesterol concentrations as above (0%, 15%, or 30% cholesterol) and tested the membrane wetting by using 2 μM fluorescently labeled AF488-HRS (Figure 4a). We observed a dramatic increase in membrane wetting with higher cholesterol concentrations (Figure 4b). We speculate that the increased wetting behavior of HRS upon higher cholesterol content in the membrane arises from the increased affinity of HRS toward PI(3)P lipids in the membrane and, therefore, the increased affinity of HRS condensates toward the membrane.

Cholesterol clusters and diffuses slower under the HRS-clathrin lattice

The surprising finding that cholesterol enhances HRS wetting on the membrane led us to speculate that HRS could promote the formation of cholesterol-rich domains. This hypothesis could be assessed with a fluorescence quenching assay, which relies on the property of the TopFluor probe to self-quench at high density due to a resonance energy transfer between neighboring probe molecules (Figure 4c)(Zhao and Lappalainen, 2012). We prepared large unilamellar vesicles with 1% PI(3)P and 30% cholesterol supplemented with 0.1% of TopFluor-cholesterol (Lipid mix 6, Supplementary table 2) and titrated these vesicles with increasing concentrations of HRS protein. We observed a decrease in a TopFluor fluorescence emission that depends on HRS concentration (Figure 4c), supporting the hypothesis that HRS clusters cholesterol. Importantly, we detected the TopFluor-cholesterol clustering both with low as well as with high HRS concentrations in conditions where HRS starts to form condensates. To test whether this clustered cholesterol could be associated with lipid domains and thus lipid phase separation, we used SLBs labeled with 1% of TopFluor-cholesterol (Lipid mix 5, Supplementary table 2) and tested if cholesterol gets enriched under HRS and clathrin. Both HRS droplets and two-dimensional condensates wetting the membrane further incubated with clathrin colocalized with enriched cholesterol domains (Figure 4d), which suggested that cholesterol-rich lipid domains are indeed forming under HRS and HRS-clathrin patches.

The clustering and phase-separation of cholesterol under HRS and clathrin coat should be associated with its reduced diffusion. We used fluorescence recovery after photobleaching (FRAP) to measure the diffusion of TopFluor-cholesterol on SLBs (Lipid mix 5, Supplementary table 2) without proteins, with HRS, and with HRS and clathrin. We first tested if the HRS concentration where the protein does not undergo condensation affects cholesterol diffusion (Figure 4e). As expected, we observed a clear decrease in cholesterol diffusion, indicated by the larger immobile fraction of TopFluor-cholesterol, in the presence of HRS compared to control measurements without proteins. This effect was even stronger in samples incubated with both HRS and clathrin (Figure 4f). Recovery halftimes of mobile cholesterol fraction, indicating the diffusion rates of mobile cholesterol, remained in the same range in all samples (Figure 4g). We then compared TopFluor-cholesterol diffusion with 2 μM HRS, where HRS forms protein condensates on SLBs

(Supplementary movie 4) (Figure 4h). Like measurements with the low HRS concentration, we again observed a clear decrease in TopFluor-cholesterol diffusion in the presence of HRS and clathrin (Figure 4h). Interestingly, in addition to the decrease in the TopFluor-cholesterol mobile fraction (Figure 4i), we also observed a significant increase in the halftime of the mobile TopFluor-cholesterol fraction (Figure 4j). This indicates that clathrin-coated HRS condensates can decrease the overall membrane fluidity and form cholesterol-rich, stable membrane domains, and supports the idea of cholesterol phase separation under HRS-clathrin patches.

Collectively, we show that when HRS and clathrin form a protein coat on the membrane, they change membrane homeostasis by enriching cholesterol under the protein coat. Cholesterol shows lower diffusion under the protein coat, which suggests that HRS and clathrin can promote the formation of cholesterol-rich, stable membrane domains. Further on, our data reveals a very intriguing feedback loop between HRS and cholesterol. While HRS promotes cholesterol clustering, increasing the concentration of cholesterol enhances HRS binding and wetting on the membrane. This mechanism could potentially give rise to distinct HRS domains on endosomes in cells.

A dense clathrin lattice on a cholesterol-rich membrane promotes membrane flattening

One of the key features of clathrin coat, especially when related to membrane trafficking, is their ability to bend the membrane. Supporting this role, the structure of the lattices that we observed using PREM on HRS droplets is primarily composed of clathrin cages. However, the clathrin lattices seen on top of the two-dimensional HRS condensates having a dense, flat appearance suggest that the physiological assembly of HRS and clathrin may be flat. Because our PREM samples are made on top of the glass, which stiffness could impose the flat appearance, we reconstituted the highest density of HRS/clathrin on GUVs, a model system where the membrane is amenable to remodeling. When we reconstituted HRS and clathrin on GUV membranes that contained up to 30% cholesterol, we did not observe any membrane deformation (Figure 3b). Membrane remodeling could be overcome by high membrane tension, which can be reduced with hyperosmotic shocks that decrease the tension of the GUV membrane (Saleem et al., 2015). Therefore, we tested the effect of hyperosmotic shocks on GUVs coated by HRS and clathrin with three different cholesterol concentrations, 0%, 15%, and 30% cholesterol, (Lipid mixes 3, 1, and 4, respectively, Supplementary table 2) to observe how cholesterol-induced increase in HRS and clathrin recruitment promotes membrane remodeling. With 0% cholesterol and 50 mOsm hyperosmotic shock, we observed a very limited recruitment of HRS and clathrin that did not induce membrane deformation (Figure 5a). Increasing the cholesterol concentration to 15% ended up with increased clathrin recruitment, but no membrane deformations were observed even in hyperosmotic conditions. It was only when HRS and clathrin were reconstituted on GUVs containing 30% cholesterol that hyperosmotic shocks induced membrane deformation (Figure 5a). These deformations, which appeared to have facets on the GUVs, giving the appearance of a broken line to the GUV contour, were previously observed with flat protein assemblies such as evolutionarily conserved ESCRT-III (Chiaruttini et al., 2015; Souza et al., 2024). This indicates that the HRS-clathrin assembly promoted by cholesterol favors the flattening of the membrane. Unlike with endocytosis-linked clathrin adaptor AP180 and clathrin that yielded prominent outward-directed budding assemblies upon hyperosmotic shocks (Saleem et al., 2015), here the membrane showed a clear flattening (Figure 5a).

Correlative cryo-electron tomography reveals extended protein coating of endosomes

Previous studies have identified flat clathrin microdomains on endosomes (Raiborg et al., 2002), which showed distinct double-layered protein lattices (Sachse et al., 2002). It was also observed that these domains were flat, a unique feature for clathrin assemblies in cells. However, because these studies utilized freeze-fracture and plastic embedding approaches to image these structures in mammalian cells, the flattening might have been by the chemical and osmotic treatments. To investigate if the propensity of HRS-clathrin assemblies to form flat lattices *in vitro* is also found in cells, we visualized endosomal clathrin lattices using cryo-electron tomography (cryo-ET), a technique well-known to preserve membrane structures close to their native state.

To target multilamellar endosomes in cultured cells, we used either HeLa cell line constitutively expressing mCherry-HRS (Migliano et al., 2023) or the heterozygous Scarlet-i3-HRS CRISPR cell line. We decided to give these cells a pulse of AlexaFluor-647 labeled EGF to locate endosomes in cells with a cryo-correlative light and electron microscopy (cryo-CLEM) approach, including cryo-ET. Using two different signals facilitated the identification of HRS-positive endosomes and eliminated possible false positives in cryo-CLEM (Figure 5 b-c). We observed a dense protein coat on the Cherry-HRS and EGF-positive endosomes. This coat extended approximately 40 - 60 nm from the membrane (Figure 5d, yellow brackets). We note that these protein coats were similar in both Cherry-HRS expressing cells and in Scarlet-i3-HRS CRISPR cells. Unlike on the GUV membrane under hyperosmotic shock, we did not observe similar flattening of the endosomal membrane under these protein lattices. However, we found these lattices in regions of low overall membrane curvature (Figure 5d), indicating that the membrane tension can counter the flattening effect of clathrin lattice in cells. When we inspected these protein densities more carefully, we observed a multilayered appearance within the coat, with a denser layer appearing 15-20 nm away from the membrane (Figure 5e, yellow arrows). These observations align with the model of a multilayered structure of ESCRT-0-positive clathrin patches on endosomes.

HRS domains on cholesterol-rich membrane cluster cargo proteins

One of the main functions of the ESCRT-0 complex is to sort ubiquitylated cargoes into intraluminal vesicles (Raiborg et al., 2002; Migliano et al., 2023; Banjade et al., 2022). Previous studies have shown that HRS works in concert with two other ubiquitin-binding proteins, STAM and Eps15, in cargo sorting (Banjade et al., 2022; Roxrud et al., 2008). Moreover, the interaction between HRS and clathrin is crucial for cargo sorting and ILV formation in cells (Wenzel et al., 2018; Migliano et al., 2023). Since HRS promotes cholesterol clustering and formation of cholesterol-rich membrane domains, which are linked to the clustering of transmembrane proteins and receptors (Wang et al., 2023), we wondered whether HRS domains promote cargo clustering without the help of its interaction partners. To test this, we used the VAMP2 protein, which was used as a transmembrane cargo model for ESCRT-0 in previous studies (Takahashi et al., 2015), as our cargo model. We covalently linked four ubiquitin moieties to the N-terminus of VAMP2 and sfGFP at its C-terminus and reconstituted it into the GUV membrane (Figure 6a). To test the effect of cholesterol domains on cargo clustering, we prepared membranes either with or without cholesterol (Lipid mixes 3 and 4, respectively, Supplementary table 2). Without HRS, the cargo protein showed homogenous distribution at GUV membranes in both tested lipid compositions (Figure 6b). When we incubated these cargo-containing GUVs with HRS, we observed a clear clustering of cargo both with and without cholesterol (Figure 6c). However, cargo clusters

appeared to be larger and more stable in membranes containing 30% cholesterol (Figure 6c, Supplementary movie 5-6), indicating that cholesterol domains stabilize cargo clusters on the membrane, most likely due to increased HRS assembly and formation of dense HRS domains. These assays thus reveal that HRS alone is sufficient to promote cargo clustering, and this clustering happens in a cholesterol-depended manner.

Discussion

The diverse roles of flat clathrin lattices in cellular processes have garnered an increase of attention during the past years (Vassilopoulos and Montagnac, 2024). How these structures are assembled in the first place remains poorly understood. Bi-layered clathrin coats on endosomes were first observed by using electron microscopy as electron-dense structures (Sachse et al., 2002; Raiborg, 2001; Raiborg et al., 2002). Here, we reconstituted these structures with minimal components to gain a comprehensive understanding of their assembly mechanism. We reveal that *in vitro* clathrin assembles on the membrane with the ESCRT-0 protein HRS as either low-density lattices or as high-density clathrin islands that depends on HRS concentration. Remarkably, cholesterol promotes HRS recruitment on the membrane both *in vitro* and in cells, and HRS in turn clusters cholesterol. This positive feedback loop between HRS recruitment and cholesterol clustering promotes the formation of stable, cholesterol-rich membrane domains coated with a dense HRS-clathrin lattice and promotes the clustering of ubiquitylated cargo proteins (Figure 6d). Our cryo-tomography data reveals that in cells HRS-clathrin lattices are found on endosomes at areas with a lower curvature and appear to be composed of two layers. This is remarkably different from clathrin structures found on the plasma membrane and consistent with previously published conventional cellular electron microscopy data (Sachse et al., 2002; Wenzel et al., 2018; Raiborg, 2001; Raiborg et al., 2002).

We show that HRS forms condensates in physiological solution and upon interaction with membranes, generates two-dimensional protein condensates where clathrin can assemble. To our knowledge, this is the first time that clathrin is shown to directly assemble on protein condensates, and thus creates a novel connection with phase-separated protein layers. We hypothesize that the unique bi-layered clathrin lattices on endosomes are formed through this unique mechanism, where clathrin is assembled onto the two-dimensional, membrane-interacting HRS condensate. Remarkably, high-density HRS-clathrin lattices could flatten the membrane *in vitro*. This is surprising because the clathrin coat is expected to promote positive membrane curvature, the phenomenon which is observed with multiple other clathrin adaptor proteins such as AP180 (Saleem et al., 2015; Ford et al., 2001), epsin (Redlingshöfer et al., 2020; Dannhauser and Ungewickell, 2012; Ford et al., 2002) , and AP-2 (Kovtun et al., 2020; Kelly et al., 2014). We speculate that cholesterol-driven recruitment of dense HRS protein layer, which shows remarkable stability with minimal lateral protein diffusion, prevents membrane deformation. Notably, the membrane flattened under the HRS-clathrin lattice only after membrane tension was decreased by hyperosmotic shock, and in isosmotic conditions, we did not observe flattening. This is consistent with our findings in cells, where our cryo-CLEM studies did not show clear flattening of the endosomal membrane under the protein coat. It is thus likely that the tension of the endosomal membrane, which at least partially arises from the constant turnover of the membrane (Saric and Freeman, 2021), prevents the flattening of the membrane in cells. In support of this conclusion, endosomal membrane flattening under the clathrin lattice is evident after chemical fixation (Sachse

et al., 2002), which often causes membrane deformation due to uncontrolled changes in membrane tension, but less after high-pressure freezing (Wenzel et al., 2018).

Our data reveals that cholesterol and HRS, together with PI(3)P, form a stable membrane microdomain that helps to cluster cargo proteins under the clathrin lattice. Our experiments with reconstituted cargo proteins showed that HRS indeed promotes cargo clustering *in vitro* and that this clustering is promoted by the presence of cholesterol. Previous studies with yeast ESCRT-0 promoting cargo condensation (Banjade et al., 2022) are aligned with our results. However, here we show that human HRS alone is sufficient to promote cargo clustering without the second ESCRT-0 protein, STAM. Moreover, cholesterol stabilizes these HRS-cargo clusters in our *in vitro* experiments. HRS clusters cholesterol and promotes the formation of a cholesterol-rich membrane domain under the protein coat. This lipid segregation induced by HRS is likely important for cargo clustering. Previous studies showed that in cells, the interaction between HRS and clathrin is crucial for sorting the cargo into ILVs (Migliano et al., 2023; Wenzel et al., 2018) , but the exact role of HRS-clathrin interaction in cargo sorting remains to be studied. In addition, how cargoes are transferred from HRS-clathrin patches to ILV remains unknown. Interestingly, overexpression of HRS in cells leads to enlarged endosomes and defects in cargo degradation (Bishop et al., 2002), while STAM recovers this cargo protein degradation phenotype (Kojima et al., 2014). Although STAM and HRS interact and form heteromeric complexes (Asao et al., 1997; Mayers et al., 2011), they also have distinct functions in cells (Zanin et al., 2023). Moreover, HRS is required for STAM localization onto endosomes but not vice versa (Bache et al., 2003; Mizuno, 2004), while STAM overexpression leads to the diffusion of HRS from the endosomal membrane (Kojima et al., 2014). We are tempted to speculate that the complex interplay between HRS and STAM might play a role in cargo release from HRS-clathrin domains into ILVs.

Previous studies linked HRS to low-density lipoprotein-derived cholesterol trafficking at endosomes, a process that seems to be distinct from its role in cargo sorting to lysosomal degradation (Du et al., 2012). Cholesterol is then released from ILVs at lysosomes by Niemann-Pick C (NPC) 1 and NPC2 proteins (Meng et al., 2020; Ikonen and Zhou, 2021; Ikonen, 2008). Cholesterol is trafficked from endosomal limiting membrane to lysosomes also via HRS-independent pathways such as by CD63 (Edgar et al., 2014; Palmulli et al., 2024). In our hands, the U18666A drug, a known inhibitor of NPC1, increased the HRS localization at endosomes, highlighting that cholesterol homeostasis is an important factor regulating vesicular trafficking in cells. Before this study, sterols had not been linked to clathrin assembly, and clathrin coat had not been shown to promote sterol-rich membrane domain formation. While sterol depletion at the plasma membrane does not seem to prevent clathrin coat formation, there is a clear link between sterols and membrane invagination in the CME (Anderson et al., 2021; Subtil et al., 1999; Rodal et al., 1999; Pichler and Riezman, 2004), which highlights the importance of sterol homeostasis in cells. It would not be surprising if cholesterol had an effect on clathrin adaptor recruitment on cellular membranes in a similar fashion to HRS, considering that the improved, phosphoinositide-dependent recruitment on the membrane was observed with other proteins (Lolicato et al., 2022). It would thus be interesting to test if clathrin adaptor proteins linked to endocytosis, long-lived plasma membrane clathrin plaques, or reticular adhesions are regulated by sterols sterols.

To conclude, we reveal a novel, cholesterol-dependent clathrin assembly mechanism on two-dimensional protein condensates, which leads to the formation of unique bi-layered ESCRT-0-clathrin patches found on multivesicular endosomes. This protein coat creates a stable, cholesterol-rich membrane domain and promotes the clustering of cargo proteins into this domain. It shows

that protein condensates in strong interactions with the membrane and membrane traffic proteins can realize all the essential functions of membrane traffic: sorting and membrane remodelling.

Methods

Plasmids and protein purification

All lipids used in this study are commercially available at Avanti Polar Lipids and are listed with their respective catalog numbers in Supplementary Table 1. The vector pCoofy17 was a gift from Sabina Suppmann (Addgene plasmid # 43991)(Scholz et al., 2013). A plasmid pCS2 HRS-RFP was a gift from Edward de Robertis (Addgene plasmid # 29685). pCoofy17 and HRS gene were linearized with PCR and subsequently assembled with sequence and ligase independent cloning approach as described in (Scholz et al., 2013). Plasmids for expression of mScarlet-i3-HRS [pET51(+)-Scarlet-i3-HRS) and 4xUbiquitin-VAMP2-sfGFP [pET28(+)-4xUb-VAMP2-sfGFP] in bacteria, and mScarlet-i3-HRS overexpression in mammalian cells [pCDNA3.1(Zeo+)-mScarlet-i3-HRS] were synthesized and cloned into the destination vector by Gene Universal Inc.

All recombinant protein expressions were done in BL21 pLysS bacteria either in standard LB media with 0.5 mM IPTG induction or in Autoinduction LB media (# AIMLB0210, Formedium). All proteins were expressed overnight at 20°C. For HRS protein purification, cells were sonicated in HRS lysis buffer (50 mM Tris-HCl, pH 8.0, 500 mM NaCl, 5 mM 2-mercaptoethanol, 300 mM L-arginine) supplemented with PMSF and c0mplete protease inhibitor cocktail (#11697498001, Roche). Soluble protein was then bound to Talon cobalt resin, washed three times with HRS lysis buffer, and then three times with HRS wash buffer (50 mM Tris-HCl, pH 8.0, 500 mM NaCl, 5 mM imidazole, 5 mM 2-mercaptoethanol, 300 mM L-arginine). HRS was cleaved from Sumo3 tag on resin with SenP2 protease in elution buffer (20 mM Tris-HCl, pH 8.0, 500 mM NaCl, 5 mM 2-mercaptoethanol, 300 mM L-arginine pH 7.4). The final protein was cleaned with a Superdex-200 size exclusion column (Cytiva) equilibrated with the elution buffer using Äkta Pure system (Cytiva). A 5% final concentration of glycerol was added to the protein before snap freezing with liquid nitrogen and storage at -80°C.

To purify VAMP2, cells were lysed in VAMP2 lysis buffer (20 mM Tris-HCl, pH 8.0, 300 mM NaCl, 0.1% Tween-20, 1% Triton X-100, 30 mM imidazole) supplemented with PMSF and c0mplete protease inhibitor cocktail (#11697498001, Roche) using sonicator. Cleared protein lysate was then bound to HisTrap 5 ml HP column and washed with 20 column volumes of VAMP lysis buffer. The protein was eluted with 300 mM imidazole in VAMP lysis buffer and subsequently cleaned with Superdex-200 size exclusion column (Cytiva) equilibrated with the VAMP2 elution buffer (Lysis buffer without imidazole) using Äkta Pure system (Cytiva). A 10% final concentration of glycerol was added to the protein before snap freezing with liquid nitrogen and storage at -80°C. Buffer (Lysis buffer without imidazole) using Äkta Pure system (Cytiva). A 10% final concentration of glycerol was added to the protein before snap freezing with liquid nitrogen and storage at -80°C.

To purify Scarlet-i3-HRS, cells were lysed in HRS lysis buffer supplemented with PMSF and a c0mplete protease inhibitor cocktail (#11697498001, Roche) using Emulsiflex. Protein was then bound to Step-Tactin XT 4Flow resin (Iba Life Sciences). The resin was then washed with HRS lysis buffer, and the protein was eluted with 5 mM biotin in HRS lysis buffer. The final protein was cleaned with Superdex-200 size exclusion column (Cytiva) equilibrated with the HRS elution buffer using Äkta Pure system (Cytiva). A 5% final concentration of glycerol was added to the protein before snap freezing with liquid nitrogen and storage at -80°C.

Clathrin from fresh bovine brains was purified with a standard protocol as described in (Ahle and Ungewickell, 1986). Purified clathrin and HRS were labeled with either AlexaFluor-488 or AlexaFluor-568 conjugated C5 maleimide (# A10254 and # A20341, respectively, Thermo Fisher Scientific Scientific) according to the manufacturer's protocol.

Reconstitution on giant unilamellar vesicles (GUV)

GUVs were prepared with the gel-assisted swelling method as described in (Weinberger et al., 2013). Shortly, PVA (MW 145000, # 8.14894.0101, Sigma-Aldrich) was dissolved at 5% (w/v) in 280 mM sucrose solution. Glass coverslips were cleaned by sonicating them sequentially in water, ethanol, acetone, 1 M KOH and finally in water. A thin layer of dissolved PVA was spread on glass and dried in a 50 °C oven for 30 min. Lipids were mixed in chloroform to the desired composition (Supplementary Table 2) at 1 mg/ml final concentration, and 10 µl of this lipid mixture was spread on PVA gel. Chloroform was then evaporated for 30 min at a 30°C vacuum oven. 500 µl of swelling buffer (20 mM HEPES, pH 7.4, 50 mM NaCl, osmolarity was adjusted with sucrose) was then added on dried lipids, and GUVs were swelled at room temperature for 30 min.

Protein binding reactions with GUVs were performed in HRS-clathrin reaction buffer (20 mM HEPES pH 7.2, 125 mM KAc, 1 mM MgAc). The osmolarity of the reaction buffer was adjusted to match the reaction buffer and GUV swelling buffer with sucrose, and osmolarity was always measured before experiments with Vapor Pressure Osmometer (Wescor). The osmolarity of the reaction buffer was increased with sucrose for hyperosmotic shock experiments. Labeled proteins were incubated with GUVs in a closed reaction chamber (Ibidi Sticky Slide IV, # 80608, Ibidi GmbH) on a cover glass passivated with either 2 mg/ml BSA in reaction buffer or with PEG-silane. Imaging was performed with a spinning disk confocal microscope (3i Intelligent Imaging Innovations) built on Nikon Eclipse C1 using a 100x 1.3 NA objective. The microscope was controlled with Slidebook 6.0.22 (3i Intelligent Imaging Innovations), and data analysis was performed using Fiji v1.54f. Final graphs were generated with OriginPro 2024b v10.1.5.132.

Reconstitution on supported lipid bilayers (SLBs)

To prepare SLBs, we mixed lipids in chloroform at the desired lipid composition (Supplementary t 2) at 0.5 mg/ml concentration and evaporated chloroform first under argon gas and then in a vacuum for 60 minutes. Lipids were then hydrated with 5 mM Hepes, pH 7.4 buffer, and subsequently mixed with silica beads (# 904384, Sigma Aldrich). Lipids and silica beads were dried in a vacuum for 30 minutes and then hydrated on plasma-cleaned coverslips attached to Ibidi Sticky Slide IV (# 80608, Ibidi GmbH) in HRS-clathrin reaction buffer (20mM HEPES pH 7.2, 125 mM KAc, 1 mM MgAc). Supported bilayers were spread on glass for 15-30 minutes, and the remaining bare glass areas were passivated with 2 mg/ml BSA in reaction buffer for 60 minutes. After the membrane was washed five times with the reaction buffer, HRS protein was added into the sample chamber in the desired concentration in the reaction buffer. In clathrin assembly assays, HRS was incubated on the membrane for 60 minutes before the sample chamber was washed five times with a reaction buffer.

The assembly of labeled HRS and clathrin was recorded using an Olympus IX83 TIRF microscope equipped with ImageEM X2 EM-CCD camera (Hamamatsu), Olympus Uapo N 100x NA 1.49 objective. The microscope was controlled with Visiview v.4.4.0.11 software (Visitron Systems). Data was analyzed with Fiji v1.54f, and final graphs were generated with OriginPro 2024b v10.1.5.132.

Platinum replica electron microscopy (PREM)
PREM samples were prepared as described above with the exception that instead of closed sample chambers, we prepared samples in open chambers, which were prepared by attaching a microscope coverslip on a round metal, homemade sample holder. After the assembly of HRS and clathrin, samples were washed five times with a reaction buffer and then fixed with 2% glutaraldehyde/2% formaldehyde solution for 30 minutes. Samples were stored in 2 % glutaraldehyde in reaction buffer for 16-40 hours until the PREM replicas were prepared. SLBs were then sequentially treated with 0.5% OsO_4, 1% tannic acid, and 1% uranyl acetate before graded ethanol dehydration and hexamethyldisilane substitution (Sigma-Aldrich). Dried samples were rotary-shadowed with 2 nm of platinum and 6 nm of carbon using a high vacuum sputter coater (Leica Microsystems). The resultant platinum replica was floated off the glass with hydrofluoric acid (5%), washed several times with distilled water, and picked up on 200 mesh formvar/carbon-coated EM grids. Replicas on EM grids were mounted in a eucentric side-entry goniometer stage of either a transmission electron microscope operated at 80 kV (model CM120; Philips) equipped with a Morada digital camera (Olympus) or a transmission electron microscope running at 120 kV (Jeol) equipped with a Xarosa digital camera (EMSYS GmbH). Images were adjusted for brightness and contrast in Adobe Photoshop (Adobe) and presented in inverted contrast.

Cholesterol clustering in large unilamellar vesicles (LUVs)
LUVs were prepared by mixing lipids at 1 mg/ml final concentration in chloroform with a composition of 29 mol% DOPC, 20 mol% DOPE, 20 mol% DOPS, 1 mol% PI(3)P, 29.5 mol% cholesterol, and 0.5 mol% TopFluor-cholesterol. Chloroform was evaporated under argon gas and then in a vacuum, and lipids were hydrated in a reaction buffer (20 mM HEPES pH 7.2, 125 mM KAc). Liposomes were then freeze-thawed 10 times with a water bath and liquid nitrogen and then extruded through 100-nm polycarbonate filters using a mini extruder (Avanti Polar Lipids). To measure TopFluor-cholesterol fluorescence quenching, the final concentration of 50 μM liposomes was mixed with the desired concentration of HRS in the reaction buffer. After 60 minutes, we measured TopFluor-cholesterol spectra between 490 nm and 550 nm with 2 nm steps using a BioTek Synergy H1 plate reader (Agilent Technologies).

Cholesterol sorting and diffusion with SLBs
SLBs with lipid composition of 29 mol% DOPC, 20 mol% DOPE, 20 mol% DOPS, 1 mol& PI(3)P, 29 mol% cholesterol and 1 mol% TopFluor-cholesterol were prepared as above. HRS at μM concentration and clathrin at 200 nM concentration were incubated with SLBs as described above. We recorded TopFluor cholesterol sorting with a Nikon Eclipse C1 spinning disk confocal microscope using a 100x 1.3 NA objective. The microscope was controlled with Slidebook 6.0.22 (3i Intelligent Imaging Innovations), and the data analysis was performed using Fiji v1.54f. Final graphs were generated with OriginPro 2024b v10.1.5.132.

To measure TopFluor-cholesterol diffusion with fluorescence recovery after the photobleaching (FRAP) approach, we prepared samples with either 500 nM or 2 μM HRS and 200 nM clathrin, as described above. We performed FRAP experiments with an Olympus IX83 TIRF microscope equipped with ImageEM X2 EM-CCD camera (Hamamatsu) and FRAP laser, using Olympus Uapo N 100x NA 1.49 objective. The microscope was controlled with Visiview v.4.4.0.11 software (Visitron Systems). We imaged a timelapse series of SLBs with a 500 ns frame rate. Before bleaching the small region of SLB, we recorded 3-5 frames, and after bleaching, we recorded 1-2 minutes until the recovery plateaued. We analyzed the data with Fiji v1.54f. Final graphs were generated with OriginPro 2024b v10.1.5.132. FRAP immobile fractions and halftimes of mobile fractions were calculated with a one-phase exponential equation:

$$y = A1 \times e^{t/\tau} + y0$$

where A is the value of y in the plateau, t is time, τ is a time constant, and y0 is the value of y when t=0.

Recovery halftimes were then calculated with the equation:

$$\text{halftime} = \tau \times ln(2)$$

Cell lines

HeLa MZ cell line was a kind gift from Stefania Vossio (ACCESS, University of Geneva). HeLa Kyoto cell line constitutively expressing mCherry-HRS was a kind gift from Harald Stenmark (Faculty of Medicine, University of Oslo). We maintained these cells in high-glucose DMEM + GlutaMax-I (# 61965-026, Thermo Fisher Scientific) supplemented with penicillin-streptomycin solution (# 15140122, Thermo Fisher Scientific), 10% fetal bovine serum (# 10270-106, Thermo Fisher Scientific) and 1 mM sodium pyruvate (# 11390070 Thermo Fisher Scientific) in 37°C and 5% CO_2 cell culture incubator.

We generated the Scarlet-i3-HRS cell line by targeting the N-terminal part of the HRS genomic locus (ID 9146) with the guide RNA: 5' –GGTGCCGCTGCCTCGCCCCATGG-3' [Protospacer Adjacent Motif Sequence (PAM) is underlined] located at the start codon in the HRS coding sequence (PAM just before start codon). The designed guide RNA was purchased from Genescript. The guide RNA was designed using Benchling (https://www.benchling.com) and double-checked using the CRISPR-Cas9 guide RNA design checker from IDT (https://www.eu.idtdna.com/site/order/designtool/index) to analyze on-target and off-target score. For this guide RNA, no significant off-targets were detected. The Homology Repair (HR) primers (sense and anti-sense) were designed to be adjacent to the start codon from the genomic sequence and with a length of 55 nucleotides each. The primers used for HR templates were: Forward and HRS-Right-Homology-Arm sense: 5'-GCGCCCGCGGCGTCGGGTTTGGGCTGGAGGTCGCCATGGATAGCACCGAGGCC GT-3'; Reverse and HRS-Left-Homology-Arm anti-sense: 5'-AGACCACCTCCTCCTAGATCGTACCCCGCTCCGTCG CCGTGGAAGCTCGCAGAGGA-3'. The DNA sequence of the right and left homology arms was 35 nucleotides, and the sequence to hybridize with the fluorescent tag was 20 nucleotides. The primers were synthesized by Microsynth AG. The fluorescent tag mScarlet-i3 was synthesized *de novo* by Genescript. This fragment was cloned into a pUC57 plasmid using EcoRI and BamHI restriction enzymes. For the generation of mScarlet-i3, the amino acid sequence was obtained from FPbase (https://www.fpbase.org), and then, by using Genescript and Benchling algorithms, the optimized DNA codon sequence was obtained for best mammalian expression. To the 3'-terminus of mScarlet-I3, a long flexible linker (69 amino acids) was added to keep the maximum functionality of the tagged protein. This linker is designed to have multiple GS-rich regions, two times the ALFA epitope (5'- CCCAGCAGACTGGAAGAGGAAC TGCGGCGGAGACT GACAGAA -3') for Western Blott detection of the inserted tag, and a TEV cleavage site (5'-GAGAACCTGTACTTTCA AGGCGCCGCTAAGTTC-3') for downstream protein purification. The following double-strand DNA fragment was inserted into the pUC57 plasmid: mScarlet-I3-GS-2xALFA-GS-TEV-GS: 5'-ATGGATAGCACCGAGGCCGTGATCAAAGAGTTCATGCGGTTCAAGGTGCACATG GAAGGCAGCATGAACGGCCACGAGTTCGAGATCGAAGGCGAAGGCGAGGGCAG ACCTTATGAGGGAACACAGACCGCCAAGCTGAAAGTGACCAAAGGCGGCCCTCTG CCTTTCAGCTGGGACATTCTGAGCCCTCAGTTTATGTACGGCAGCCGGGCCTTCAT CAAGCACCCTGCCGATATTCCCGACTACTGGAAGCAGAGCTTCCCCGAGGGCTTC AAGTGGGAGAGAGTGATGATCTTCGAGGACGGCGGCACCGTGTCTGTGACCCAG GATACAAGCCTGGAAGATGGCACCCTGATCTACAAAGTGAAGCTGAGAGGCGGC AACTTCCCTCCTGATGGCCCCGTGATGCAGAAAAGAACCATGGGCTGGGAAGCCA

GCACCGAGAGACTGTACCCTGAGGACGTGGTGCTGAAGGGCGACATCAAGATGG
CCCTGAGACTGAAGGATGGCGGCAGATACCTGGCCGACTTCAAGACCACCTACAA
GGCCAAGAAACCCGTGCAGATGCCAGGCGCCTTCAACATCGACCGGAAGCTGGAT
ATCACCAGCCACAACGAGGACTACACCGTGGTGGAACAGTACGAGAGAAGCGTG
GCCAGACACAGCACAGGTGGAAGCGGAGGATCTTCCTCAACTGGTGGTGGAGGT
TCTAGTCCCAGCAGACTGGAAGAGGAACTGCGGCGGAGACTGACAGAAGGCGGC
GGAGGATCTTCTGGCCCTTCTGGATCTAGCAGCCCCTCCAGGCTGGAGGAAGAAC
TGAGAAGAAGGCTGACCGAGGAGAACCTGTACTTTCAAGGCGCCGCTAAGTTCA
GCTCTGGTGGAGGAGGATCTAGC -3'.

For the generation of the double-strand DNA Donor Template, we produced PCR cassettes using the plasmid generated before together with the HR Right-Left primers to amplify the tag with the 35 nucleotide-Homology Arms. For the PCR amplification, the PrimeSTAR Max DNA Polymerase kit (#R045A) from Takara was used. For the purification of the PCR product, the QIAquick PCR and gel Cleanup kit (28506) from Qiagen was used. HeLa MZ cells were seeded into a 24-well plate at $1x10^5$ cells/mL without antibiotics one day before transfection. We used the Lipofectamine CRISPRMAX Cas9 (CMAX00008) as a Transfection Reagent from Thermofisher, and we followed the manufacturer's indications for the transfection. Together with the transfection system, we used the purified GenCrispr NLS-Cas9-EGFP Nuclease (Z03467) from Genescript, the guide RNA designed to target HRS, and the HR PCR cassettes generated as a template (500 ng/well). Just before adding the Cas9/gRNA complex, the media was replaced with new media without antibiotics, and Alt-R HDR Enhancer V2 (10007921) from Integrated DNA Technologies to increase the chances of Homology-Directed Repair events after the DNA double-strand break by the Cas9 nuclease. One day later, the media was replaced for new media with antibiotics. To obtain single-cell clones of mScarlet-I3-HRS Knock-In, cells were subjected to FACS, and single cells were deposited in a well of a 96-well plate. For the validation of the cell lines, clones were genotyped via Western Blot using anti-HRS and anti-ALFA antibodies (see Supplementary Table 3), fluorescent microscopy, and PCR using the following primers: HRS Forward 5'-GTTCTTAGGGCTCATTGTTCCA-3' targeting the 5'-UTR, and therefore, before the start codon; and HRS Reverse 5'-AGTTCACTCTGTGGAAGGAACG-3' targeting the HRS coding sequence after the start codon. For the genomic DNA extraction, the QIAamp DNA Mini kit (51304) from Qiagen was used. Final validation was performed, followed by sequencing PCR amplified regions to check the correct insertion of the tag using Microsynth AG sequencing service.

Immunofluorescence staining and imaging

For immunofluorescence microscopy, we cultured cells on Poly-D-Lysine (# A3890401, Thermo Fisher Scientific) coated coverslips, washed cells two times with PBS and then fixed them for 15 minutes in room temperature with 4% formaldehyde solution in PBS. Cells were washed three times with 0.2% saponin in PBS, then permeabilized and blocked with 3% BSA, 100 mM glycine, and 0.2% saponin in PBS for 1 hour and then incubated overnight with primary antibodies (see Supplementary table 3 for dilutions) in 1% BSA, 0.2% saponin in PBS at +4°C. Cells were then washed three times with saponin-PBS solution and incubated for 1 hour at room temperature with secondary antibodies (Supplementary table 3) in 1% BSA 0.2% saponin in PBS. Before mounting the coverslips on microscope slides with ProLong Glass Antifade Mountant (# P36982, Thermo Fisher Scientific), cells were washed two times with PBS and once with water. We imaged cells with a Stellaris 8 Falcon (Leica) confocal microscope equipped with Lightning using a 60x oil objective.

Filipin staining for HeLa Scarlet-i3-HRS cells cultured on Poly-D-lysine coated coverslips was done after cells were fixed for 15 minutes with 4% formaldehyde in PBS. Cells were then washed three times with PBS, and 50 μg/ml Filipin (# F9765, Sigma-Aldrich) in PBS was incubated on cells for 30 minutes at room temperature. Samples were mounted on microscope slides with ProLong Glass Antifade Mountant, and samples were imaged during the same day with a Stellaris 8 Falcon (Leica) confocal microscope equipped with Lightning using a 60x oil objective.

High-content imaging

To modify cholesterol amounts in the endo-lysosomal pathway, cells were treated with U18666A (# 3633, Sigma-Aldrich) or Methyl-b-cyclodextrin (MbCD, # C4555, Sigma-Aldrich). For the U18666A treatment, cells were cultured on normal media. The following day, 3 μg/ml of U18666A in normal cell culture media was added to cells, and cells were cultured for 24 hours before they were fixed with 4% formaldehyde in PBS. For MbCD treatment, cells were first cultured in normal cell culture media. The following day, cells were washed twice with serum-free DMEM, and 0.7 μM MbCD in serum-free DMEM was added to the cells. After 24 hours of incubation, cells were fixed as above. Cholesterol amounts at the endo-lysosomal pathway were verified with Filipin staining.

For high-content imaging, cells were cultured in μ-Plate 96 well plates (# 89626, Ibidi GmbH) and stained as described above. Hoechts 33342 staining (1:10,000 dilution, # H3570, Thermo Fisher Scientific) was performed at the same time with a secondary antibody staining. Cells were imaged with ImageXpress automated spinning disk confocal microscope (Molecular Devices) equipped with an sCMOS camera. Cells were segmented and analyzed with CellProfiler. Final graphs were generated with OriginPro 2024b v10.1.5.132.

Epidermal growth factor (EGF) pulse-chase

We performed the EGF pulse-chase experiment as described in (Wenzel et al., 2018). Shortly, HeLa Scarler-i3-HRS cells were cultured on Poly-D-lysine coated coverslips, and 50 ng/ml AlexaFluor-647 EGF (# E35351, Thermo Fisher Scientific) in normal cell culture media was incubated with cells for 2 minutes in +37°C. Cells were then washed twice with normal cell culture media and incubated for 5, 15, 30, and 45 minutes in normal cell culture media at 37°C before the fixation with 4% formaldehyde solution in PBS. Cells were then washed three times with PBS before coverslips were mounted on microscope slides as described above. Confocal imaging was done as described above, and colocalization of AlexaFluor-646 EGF with Scarlet-i3-HRS was analyzed with Fiji v1.54f using BIOP JaCoP plugin (https://github.com/BIOP/ijp-jacop-b). Final graphs were generated with OriginPro 2024b v10.1.5.132.

Cryogenic electron tomography (Cryo-ET)

HeLa cells stably expressing either HRS-mScarlet or HRS-mCherry were grown on 200 mesh gold EM grids with a holey carbon film R2/2 (Quantifoil). Cells were incubated with 50 ng/ml EGF-Alexa 647. After allowing internalization of the cargo for 15 minutes at 37°C, the remaining EGF-Alexa 647 was washed away with cell culture media. The EM grids were vitrified using a manual plunger with a cryostat (Russo et al., 2016) between 7 and 12 minutes after the removal of EGF-Alexa 647 and were backside-blotted for 12 seconds using Whatman No.1 filter paper.

Thin lamellae of HeLa cells expressing HRS-mScarlet or HRS-mCherry were obtained by cryo-FIB milling in an Aquilos 2 Cryo-FIB (Thermo Fisher Scientific). The microscope is equipped with an integrated fluorescence light microscope (iFLM), allowing performing cryo fluorescence microscopy (cryoFM) on the final lamella. Grids were subjected to GIS coating for 1 minute and

30 seconds. Lamellae were prepared using standard semi-automated protocols. Eucentricity, the finding of milling angles, stress relief cuts, and rough and medium milling steps were performed with the AutoTEM Cryo software in an automatic manner (Thermo Fisher Scientific). After assessing the medium-milled lamella for signals of interest by iFLM, the final polishing to a target thickness of 200-250 nm was performed manually. The final lamellae were again subjected to cryoFM to identify regions for further analysis. The z-stacks acquired with iFLM were then used to correlate with the electron microscopy map in order to target the regions containing HRS or EGF signals for cryo electron tomography (cryoET).

Cryo-ET data of cryo-FIB-milled cells was acquired on a Krios G4 C-FEG cryo-TEM operated at 300kV equipped with a Falcon 4 detector used in counting mode and a Selectris energy filter. The data acquisition was performed with Tomography 5 Software (Thermo Fisher Scientific). Lamellae maps were acquired at a defocus of -60 µm and a pixel size of 53.7 A°. Tilt series were acquired with a dose-symmetric tilt scheme (REF Hagen, Briggs 2017) in groups of 4 between -60° and 60°C at an increment of 1° and a pixel size of 2.97 Å. It is to be noted that some tilt series were not acquired at the full range between -60° and 60°C. A dose of approximately 1 e-/A°2 was applied per tilt. The target defocus was -5 µm. The alignment of the tilt series was performed with IMOD using patch tracking. The tomograms were then SIRT reconstructed at bin 2 using IMOD. For visualization purposes, a 3D media filter was applied to the reconstructed tomograms.

Cargo protein reconstitution and sorting

LUVs with and without cholesterol (29.9 mol% DOPC, 20 mol% DOPE, 20 mol% DOPS, 1 mol& PI(3)P, 30 mol% cholesterol and 0.1 mol% Atto647-DOPE and 69.9 mol% DOPC, 20 mol% DOPE, 20 mol% DOPS, 1 mol& PI(3)P, and 0.1 mol% Atto647-DOPE), respectively, were used to reconstitute SfGFP-VAMP2-4xUb produced recombinantly, as previously performed with other transmembrane proteins (Espadas et al., 2019)(Figure 6a). Briefly, LUVs were initially incubated in the presence of 0.1% Triton X100 for 30 minutes (Figure 6a, step 1). Detergen-destabilized liposomes were then mixed with purified protein at a protein:lipid molar ratio of 1:500 (Figure 6a, step 2). After 30 minutes of incubation at room temperature with gentle agitation, the Triton X100 detergent was removed using BioBeads SM-2 adsorbent (BioRad) by four consecutive additions to the proteo-lipid mixture every hour, followed by an overnight incubation (Rigaud, Levy 1995 Biochim. Biophys. Acta) (Figure 6a, step 3). The sample was then spin-down to remove the BioBeads and non-incorporated protein, and the supernatant containing the proteoliposomes was collected.

To perform the GUVs with reconstituted protein, proteoliposomes were dialyzed against a 25 mM HEPES and 1 mM Trehalose solution for 2 hours. After dialysis, 15 µl of the freshly dialyzed sample was placed on a clean parafilm surface and mixed with 2 µl of 40 um silica beads (Microspheres-Nanospheres, USA), and then dried in a vacuum chamber for at least 1 hour. The dried beads covered with the proteo-lipid layers were then transferred to a tube containing 10 µl of 1M Trehalose solution for 15 min at 65 °C. Next, the 10 µl containing the pre-hydrated proteo-lipid lamellas were transferred to the observation chamber containing the working buffer (20 mM HEPES, pH 7.2, 125 mM KAc, 1 mM MgAc) for complete proteo-GUVs hydration (Figure 6a, step 4). Lastly, mScarlet-i3-HRS at a final concentration of 400 nM was added to the microscopy chamber and incubated for 30 min before starting the imaging, using a spinning-disk Nikon Ti-Eclipse.

Authors contributions

M.H., S.B.M., I.G., C.B.S., J.E., and S.V. carried out experiments and data analysis. W.K., S.V., M.K., and A.R. contributed to experiment planning and supervised the work. M.H., M.K., and A.R. conceived the study and planned experiments. M.H. and A.R. wrote the manuscript with input from all authors.

Acknowledgments

We are grateful to Jean Gruenberg, Stefania Vossio, and Elina Ikonen for thoughtful discussions about the role of cholesterol in vesicle trafficking. Andrea Picco is acknowledged for technical support in TIRF imaging, and Rafael Ferreira Caetano and Frédéric Humbert for protein purification. We thank Roux and Kaksonen labs for technical support and helpful discussions. We thank the Photonic Light Microscopy Facility and ACCESS Facility at the Univerity of Geneva, the Microscopy Imaging Center (MIC) of the University of Bern, the Dubochet Center for Imaging (DCI) Bern, and IBPS electron microscopy platform at Sorbonne University in Paris for microscope access and support with data collection. AR acknowledges funding from the Swiss National Fund for Research grant numbers #CRSII5_189996 and #310030_200793 and the European Research Council Synergy grant number #951324-R2-TENSION. This work was supported by EMBO (ALTF 703-2020 for M.H., and 989-2022 for J.E.), Fundación Alfonso Martín Escudero (Postdoctoral fellowship for C.B-S.), and Swiss National Science Foundation grant (310030_212288) for MK. Work in the group of W.K. was supported by the University of Bern and the SNSF project 201158. We would also like to acknowledge funding by the *Agence Nationale pour la Recherche* (ANR-20-CE13-0024-01, ANR-21-CE13-0018-01 to SV), Horizon Europe "DREAMS" project under grant agreement N°101080229, Sorbonne Université, INSERM, Association Institut de Myologie core funding to S.V.

References

Ahle, S., and E. Ungewickell. 1986. Purification and properties of a new clathrin assembly protein. *The EMBO Journal*. 5:3143–3149. doi:10.1002/j.1460-2075.1986.tb04621.x.

Anderson, R.H., K.A. Sochacki, H. Vuppula, B.L. Scott, E.M. Bailey, M.M. Schultz, J.G. Kerkvliet, J.W. Taraska, A.D. Hoppe, and K.R. Francis. 2021. Sterols lower energetic barriers of membrane bending and fission necessary for efficient clathrin-mediated endocytosis. *Cell Reports*. 37:110008. doi:10.1016/j.celrep.2021.110008.

Asao, H., Y. Sasaki, T. Arita, N. Tanaka, K. Endo, H. Kasai, T. Takeshita, Y. Endo, T. Fujita, and K. Sugamura. 1997. Hrs Is Associated with STAM, a Signal-transducing Adaptor Molecule. *Journal of Biological Chemistry*. 272:32785–32791. doi:10.1074/jbc.272.52.32785.

Avinoam, O., M. Schorb, C.J. Beese, J.A.G. Briggs, and M. Kaksonen. 2015. Endocytic sites mature by continuous bending and remodeling of the clathrin coat. *Science*. 348:1369–1372. doi:10.1126/science.aaa9555.

Bache, K.G., C. Raiborg, A. Mehlum, and H. Stenmark. 2003. STAM and Hrs Are Subunits of a Multivalent Ubiquitin-binding Complex on Early Endosomes. *Journal of Biological Chemistry*. 278:12513–12521. doi:10.1074/jbc.M210843200.

Banani, S.F., H.O. Lee, A.A. Hyman, and M.K. Rosen. 2017. Biomolecular condensates: organizers of cellular biochemistry. *Nat Rev Mol Cell Biol*. 18:285–298. doi:10.1038/nrm.2017.7.

Banjade, S., and M.K. Rosen. 2014. Phase transitions of multivalent proteins can promote clustering of membrane receptors. *eLife*. 3:e04123. doi:10.7554/eLife.04123.

Banjade, S., L. Zhu, J.R. Jorgensen, S.W. Suzuki, and S.D. Emr. 2022. Recruitment and organization of ESCRT-0 and ubiquitinated cargo via condensation. *SCIENCE ADVANCES*.

Bergeron-Sandoval, L.-P., S. Kumar, H.K. Heris, C.L.A. Chang, C.E. Cornell, S.L. Keller, P. François, A.G. Hendricks, A.J. Ehrlicher, R.V. Pappu, and S.W. Michnick. 2021. Endocytic proteins with prion-like domains form viscoelastic condensates that enable membrane remodeling. *Proc. Natl. Acad. Sci. U.S.A.* 118:e2113789118. doi:10.1073/pnas.2113789118.

Bigay, J., and B. Antonny. 2012. Curvature, Lipid Packing, and Electrostatics of Membrane Organelles: Defining Cellular Territories in Determining Specificity. *Developmental Cell*. 23:886–895. doi:10.1016/j.devcel.2012.10.009.

Bishop, N., A. Horman, and P. Woodman. 2002. Mammalian class E vps proteins recognize ubiquitin and act in the removal of endosomal protein–ubiquitin conjugates. *The Journal of Cell Biology*. 157:91–102. doi:10.1083/jcb.200112080.

Brangwynne, C.P., P. Tompa, and R.V. Pappu. 2015. Polymer physics of intracellular phase transitions. *Nature Phys*. 11:899–904. doi:10.1038/nphys3532.

Bussi, C., A. Mangiarotti, C. Vanhille-Campos, B. Aylan, E. Pellegrino, N. Athanasiadi, A. Fearns, A. Rodgers, T.M. Franzmann, A. Šarić, R. Dimova, and M.G. Gutierrez. 2023. Stress granules plug and stabilize damaged endolysosomal membranes. *Nature*. 623:1062–1069. doi:10.1038/s41586-023-06726-w.

Chiaruttini, N., L. Redondo-Morata, A. Colom, F. Humbert, M. Lenz, S. Scheuring, and A. Roux. 2015. Relaxation of Loaded ESCRT-III Spiral Springs Drives Membrane Deformation. *Cell*. 163:866–879. doi:10.1016/j.cell.2015.10.017.

Dannhauser, P.N., M. Platen, H. Böning, and I.A.T. Schaap. 2015. Durable protein lattices of clathrin that can be functionalized with nanoparticles and active biomolecules. *Nature Nanotechnology*. 10:954–957. doi:10.1038/nnano.2015.206.

Dannhauser, P.N., and E.J. Ungewickell. 2012. Reconstitution of clathrin-coated bud and vesicle formation with minimal components. *Nature Cell Biology*. 14:634–639. doi:10.1038/ncb2478.

Day, K.J., G. Kago, L. Wang, J.B. Richter, C.C. Hayden, E.M. Lafer, and J.C. Stachowiak. 2021. Liquid-like protein interactions catalyse assembly of endocytic vesicles. *Nat Cell Biol*. 23:366–376. doi:10.1038/s41556-021-00646-5.

Du, X., A.S. Kazim, A.J. Brown, and H. Yang. 2012. An Essential Role of Hrs/Vps27 in Endosomal Cholesterol Trafficking. *Cell Reports*. 1:29–35. doi:10.1016/j.celrep.2011.10.004.

Edgar, J.R., E.R. Eden, and C.E. Futter. 2014. Hrs- and CD63-dependent competing mechanisms make different sized endosomal intraluminal vesicles. *Traffic*. 15:197–211. doi:10.1111/tra.12139.

Elkhatib, N., E. Bresteau, F. Baschieri, A.L. Rioja, G. Van Niel, S. Vassilopoulos, and G. Montagnac. 2017. Tubular clathrin/AP-2 lattices pinch collagen fibers to support 3D cell migration. *Science*. 356:eaal4713. doi:10.1126/science.aal4713.

Espadas, J., D. Pendin, R. Bocanegra, A. Escalada, G. Misticoni, T. Trevisan, A. Velasco Del Olmo, A. Montagna, S. Bova, B. Ibarra, P.I. Kuzmin, P.V. Bashkirov, A.V. Shnyrova, V.A. Frolov, and A. Daga. 2019. Dynamic constriction and fission of endoplasmic reticulum membranes by reticulon. *Nat Commun*. 10:5327. doi:10.1038/s41467-019-13327-7.

Ford, M.G.J., I.G. Mills, B.J. Peter, Y. Vallis, G.J.K. Praefcke, P.R. Evans, and H.T. McMahon. 2002. Curvature of clathrin-coated pits driven by epsin. *Nature*. 419:361–366. doi:10.1038/nature01020.

Ford, M.G.J., B.M.F. Pearse, M.K. Higgins, Y. Vallis, D.J. Owen, A. Gibson, C.R. Hopkins, P.R. Evans, and H.T. McMahon. 2001. Simultaneous binding of PtdIns (4,5) P2 and clathrin by AP180 in the nucleation of clathrin lattices on membranes. *Science*. 291:1051–1055. doi:10.1126/science.291.5506.1051.

Gillooly, D.J. 2000. Localization of phosphatidylinositol 3-phosphate in yeast and mammalian cells. *The EMBO Journal*. 19:4577–4588. doi:10.1093/emboj/19.17.4577.

Hakanpää, L., A. Abouelezz, A.-S. Lenaerts, S. Culfa, M. Algie, J. Bärlund, P. Katajisto, H. McMahon, and L. Almeida-Souza. 2023. Reticular adhesions are assembled at flat clathrin lattices and opposed by active integrin α5β1. *Journal of Cell Biology*. 222:e202303107. doi:10.1083/jcb.202303107.

Heuser, J. 1980. Three-dimensional visualization of coated vesicle formation in fibroblasts. *The Journal of cell biology*. 84:560–583. doi:10.1083/jcb.84.3.560.

Huang, W.Y.C., Q. Yan, W.-C. Lin, J.K. Chung, S.D. Hansen, S.M. Christensen, H.-L. Tu, J. Kuriyan, and J.T. Groves. 2016. Phosphotyrosine-mediated LAT assembly on membranes drives kinetic bifurcation in recruitment dynamics of the Ras activator SOS. *Proc. Natl. Acad. Sci. U.S.A.* 113:8218–8223. doi:10.1073/pnas.1602602113.

Ikonen, E. 2008. Cellular cholesterol trafficking and compartmentalization. *Nat Rev Mol Cell Biol*. 9:125–138. doi:10.1038/nrm2336.

Ikonen, E. 2018. Mechanisms of cellular cholesterol compartmentalization: recent insights. *Current Opinion in Cell Biology*. 53:77–83. doi:10.1016/j.ceb.2018.06.002.

Ikonen, E., and X. Zhou. 2021. Cholesterol transport between cellular membranes: A balancing act between interconnected lipid fluxes. *Developmental Cell*. 56:1430–1436. doi:10.1016/j.devcel.2021.04.025.

Kaksonen, M., and A. Roux. 2018. Mechanisms of clathrin-mediated endocytosis. *Nature Reviews Molecular Cell Biology*. 19:313–326. doi:10.1038/nrm.2017.132.

Kelly, B.T., S.C. Graham, N. Liska, P.N. Dannhauser, S. Höning, E.J. Ungewickell, and D.J. Owen. 2014. AP2 controls clathrin polymerization with a membrane-activated switch. *Science*. 345:459–463. doi:10.1126/science.1254836.

Kilsdonk, E.P.C., P.G. Yancey, G.W. Stoudt, F.W. Bangerter, W.J. Johnson, M.C. Phillips, and G.H. Rothblat. 1995. Cellular Cholesterol Efflux Mediated by Cyclodextrins. *Journal of Biological Chemistry*. 270:17250–17256. doi:10.1074/jbc.270.29.17250.

Kim, Y., and C.G. Burd. 2023. Lipid Sorting and Organelle Identity. *Cold Spring Harb Perspect Biol*. 15:a041397. doi:10.1101/cshperspect.a041397.

Kojima, K., Y. Amano, K. Yoshino, N. Tanaka, K. Sugamura, and T. Takeshita. 2014. ESCRT-0 Protein Hepatocyte Growth Factor-regulated Tyrosine Kinase Substrate (Hrs) Is Targeted to Endosomes Independently of Signal-transducing Adaptor Molecule (STAM) and the Complex Formation with STAM Promotes Its Endosomal Dissociation. *Journal of Biological Chemistry*. 289:33296–33310. doi:10.1074/jbc.M114.578245.

Kovtun, O., V.K. Dickson, B.T. Kelly, D.J. Owen, and J.A.G. Briggs. 2020. Architecture of the AP2/clathrin coat on the membranes of clathrin-coated vesicles. *Sci. Adv.* 6:eaba8381. doi:10.1126/sciadv.aba8381.

Kozak, M., and M. Kaksonen. 2022. Condensation of Ede1 promotes the initiation of endocytosis. *eLife*. 11:e72865. doi:10.7554/eLife.72865.

Kukulski, W., M. Schorb, M. Kaksonen, and J.A.G. Briggs. 2012. Plasma membrane reshaping during endocytosis is revealed by time-resolved electron tomography. *Cell*. 150:508–520. doi:10.1016/j.cell.2012.05.046.

Lee, I.-H., M.Y. Imanaka, E.H. Modahl, and A.P. Torres-Ocampo. 2019. Lipid Raft Phase Modulation by Membrane-Anchored Proteins with Inherent Phase Separation Properties. *ACS Omega*. 4:6551–6559. doi:10.1021/acsomega.9b00327.

Liscum, L., and J.R. Faust. 1989. The intracellular transport of low density lipoprotein-derived cholesterol is inhibited in Chinese hamster ovary cells cultured with 3-β-[2-(diethylamino)ethoxy]androst-5-en-17-one. *Journal of Biological Chemistry*. 264:11796–11806. doi:10.1016/S0021-9258(18)80136-3.

Liu, S.-H., M.L. Wong, C.S. Craik, and F.M. Brodsky. 1995. Regulation of clathrin assembly and trimerization defined using recombinant triskelion hubs. *Cell*. 83:257–267. doi:10.1016/0092-8674(95)90167-1.

Lock, J.G., F. Baschieri, M.C. Jones, J.D. Humphries, G. Montagnac, S. Strömblad, and M.J. Humphries. 2019. Clathrin-containing adhesion complexes. *The Journal of Cell Biology*. 218:2086–2095. doi:10.1083/jcb.201811160.

Lolicato, F., R. Saleppico, A. Griffo, A. Meyer, F. Scollo, B. Pokrandt, H.-M. Müller, H. Ewers, H. Hähl, J.-B. Fleury, R. Seemann, M. Hof, B. Brügger, K. Jacobs, I. Vattulainen, and W. Nickel. 2022. Cholesterol promotes clustering of PI(4,5)P2 driving unconventional secretion of FGF2. *Journal of Cell Biology*. 221:e202106123. doi:10.1083/jcb.202106123.

Mangiarotti, A., N. Chen, Z. Zhao, R. Lipowsky, and R. Dimova. 2023a. Wetting and complex remodeling of membranes by biomolecular condensates. *Nat Commun*. 14:2809. doi:10.1038/s41467-023-37955-2.

Mangiarotti, A., K.V. Schmidt, R. Lipowsky, and R. Dimova. 2024. Lipid packing and cholesterol content regulate membrane wetting by biomolecular condensates. doi:10.1101/2024.07.15.603610.

Mangiarotti, A., M. Siri, N.W. Tam, Z. Zhao, L. Malacrida, and R. Dimova. 2023b. Biomolecular condensates modulate membrane lipid packing and hydration. *Nat Commun*. 14:6081. doi:10.1038/s41467-023-41709-5.

Mayers, J.R., I. Fyfe, A.L. Schuh, E.R. Chapman, J.M. Edwardson, and A. Audhya. 2011. ESCRT-0 assembles as a heterotetrameric complex on membranes and binds multiple ubiquitinylated cargoes simultaneously. *Journal of Biological Chemistry*. 286:9636–9645. doi:10.1074/jbc.M110.185363.

Meng, Y., S. Heybrock, D. Neculai, and P. Saftig. 2020. Cholesterol Handling in Lysosomes and Beyond. *Trends in Cell Biology*. 30:452–466. doi:10.1016/j.tcb.2020.02.007.

Migliano, S.M., S.W. Schultz, E.M. Wenzel, S. Takáts, D. Liu, S. Mørk, K.W. Tan, T.E. Rusten, C. Raiborg, and H. Stenmark. 2023. Removal of hypersignaling endosomes by simaphagy. *Autophagy*. 1–23. doi:10.1080/15548627.2023.2267958.

Mizuno, E. 2004. Association with Hrs Is Required for the Early Endosomal Localization, Stability, and Function of STAM. *Journal of Biochemistry*. 135:385–396. doi:10.1093/jb/mvh046.

Palmulli, R., M. Couty, M.C. Piontek, M. Ponnaiah, F. Dingli, F.J. Verweij, S. Charrin, M. Tantucci, S. Sasidharan, E. Rubinstein, A. Kontush, D. Loew, M. Lhomme, W.H. Roos, G. Raposo, and G. Van Niel. 2024. CD63 sorts cholesterol into endosomes for storage and distribution via exosomes. *Nat Cell Biol*. doi:10.1038/s41556-024-01432-9.

Pichler, H., and H. Riezman. 2004. Where sterols are required for endocytosis. *Biochimica et Biophysica Acta (BBA) - Biomembranes*. 1666:51–61. doi:10.1016/j.bbamem.2004.05.011.

Raiborg, C. 2001. Hrs recruits clathrin to early endosomes. *The EMBO Journal*. 20:5008–5021. doi:10.1093/emboj/20.17.5008.

Raiborg, C., K.G. Bache, D.J. Gillooly, I.H. Madshus, E. Stang, and H. Stenmark. 2002. Hrs sorts ubiquitinated proteins into clathrin-coated microdomains of early endosomes. *Nat Cell Biol*. 4:394–398. doi:10.1038/ncb791.

Raiborg, C., Bremnes, Bjørn, Mehlum Anja, Gillooly, David J., D'Arrigo, Antonello, Stang, Espen, and Stenmark, Harald. 2001. FYVE and coiled-coil domains determine the specific localisation of Hrs to early endosomes. *Journal of Cell Science*. 114:2255–2263.

Raiborg, C., and H. Stenmark. 2009. The ESCRT machinery in endosomal sorting of ubiquitylated membrane proteins. *Nature*. 458:445–452. doi:10.1038/nature07961.

Ravindran, R., and S.W. Michnick. 2024. Biomolecular condensates as drivers of membrane trafficking and remodelling. *Current Opinion in Cell Biology*. 89:102393. doi:10.1016/j.ceb.2024.102393.

Redlingshöfer, L., F. McLeod, Y. Chen, M.D. Camus, J.J. Burden, E. Palomer, K. Briant, P.N. Dannhauser, P.C. Salinas, and F.M. Brodsky. 2020. Clathrin light chain diversity regulates membrane deformation in vitro and synaptic vesicle formation in vivo. *Proc. Natl. Acad. Sci. U.S.A.* 117:23527–23538. doi:10.1073/pnas.2003662117.

Rodal, S.K., G. Skretting, Ø. Garred, F. Vilhardt, B. van Deurs, and K. Sandvig. 1999. Extraction of Cholesterol with Methyl-ᴺL-Cyclodextrin Perturbs Formation of Clathrin-coated Endocytic Vesicles. *Molecular Biology of the Cell.* 10.

Roxrud, I., C. Raiborg, N.M. Pedersen, E. Stang, and H. Stenmark. 2008. An endosomally localized isoform of Eps15 interacts with Hrs to mediate degradation of epidermal growth factor receptor. *Journal of Cell Biology*. 180:1205–1218. doi:10.1083/jcb.200708115.

Russo, C.J., S. Scotcher, and M. Kyte. 2016. A precision cryostat design for manual and semi-automated cryo-plunge instruments. *Review of Scientific Instruments*. 87:114302. doi:10.1063/1.4967864.

Sachse, M., S. Urbé, V. Oorschot, G.J. Strous, and J. Klumperman. 2002. Bilayered Clathrin Coats on Endosomal Vacuoles Are Involved in Protein Sorting toward Lysosomes. *MBoC*. 13:1313–1328. doi:10.1091/mbc.01-10-0525.

Saleem, M., S. Morlot, A. Hohendahl, J. Manzi, M. Lenz, and A. Roux. 2015. A balance between membrane elasticity and polymerization energy sets the shape of spherical clathrin coats. *Nature Communications*. 6:e6249. doi:10.1038/ncomms7249.

Saric, A., and S.A. Freeman. 2021. Endomembrane Tension and Trafficking. *Front. Cell Dev. Biol.* 8:611326. doi:10.3389/fcell.2020.611326.

Scholz, J., H. Besir, C. Strasser, and S. Suppmann. 2013. A new method to customize protein expression vectors for fast, efficient and background free parallel cloning. *BMC biotechnology*. 13:12. doi:10.1186/1472-6750-13-12.

Snead, W.T., and A.S. Gladfelter. 2019. The Control Centers of Biomolecular Phase Separation: How Membrane Surfaces, PTMs, and Active Processes Regulate Condensation. *Molecular Cell.* 76:295–305. doi:10.1016/j.molcel.2019.09.016.

Sochacki, K.A., and J.W. Taraska. 2019. From Flat to Curved Clathrin: Controlling a Plastic Ratchet. *Trends in Cell Biology*. 29:241–256. doi:10.1016/j.tcb.2018.12.002.

Souza, D.P., J. Espadas, S. Chaaban, E.R.R. Moody, T. Hatano, M. Balasubramanian, T.A. Williams, A. Roux, and B. Baum. 2024. Evolutionarily conserved principles of ESCRT-III-mediated membrane remodelling revealed by a two-subunit Asgard archaeal system. doi:10.1101/2024.07.01.601590.

Subtil, A., I. Gaidarov, K. Kobylarz, M.A. Lampson, J.H. Keen, and T.E. McGraw. 1999. Acute cholesterol depletion inhibits clathrin-coated pit budding. *Proc. Natl. Acad. Sci. U.S.A.* 96:6775–6780. doi:10.1073/pnas.96.12.6775.

Takahashi, H., J.R. Mayers, L. Wang, J.M. Edwardson, and A. Audhya. 2015. Hrs and STAM Function Synergistically to Bind Ubiquitin-Modified Cargoes In Vitro. *Biophysical Journal.* 108:76–84. doi:10.1016/j.bpj.2014.11.004.

Urbé, S., I.G. Mills, H. Stenmark, N. Kitamura, and M.J. Clague. 2000. Endosomal localization and receptor dynamics determine tyrosine phosphorylation of hepatocyte growth factor-regulated tyrosine kinase substrate. *Mol Cell Biol.* 20:7685–7692. doi:10.1128/MCB.20.20.7685-7692.2000.

Van Meer, G., D.R. Voelker, and G.W. Feigenson. 2008. Membrane lipids: where they are and how they behave. *Nat Rev Mol Cell Biol.* 9:112–124. doi:10.1038/nrm2330.

Vassilopoulos, S., and G. Montagnac. 2024. Clathrin assemblies at a glance. *Journal of Cell Science*. 137:jcs261674. doi:10.1242/jcs.261674.

Vietri, M., M. Radulovic, and H. Stenmark. 2020. The many functions of ESCRTs. *Nat Rev Mol Cell Biol*. 21:25–42. doi:10.1038/s41580-019-0177-4.

Wang, H.-Y., S.H. Chan, S. Dey, I. Castello-Serrano, M.K. Rosen, J.A. Ditlev, K.R. Levental, and I. Levental. 2023. Coupling of protein condensates to ordered lipid domains determines functional membrane organization. *SCIENCE ADVANCES*.

Weinberger, A., F.C. Tsai, G.H. Koenderink, T.F. Schmidt, R. Itri, W. Meier, T. Schmatko, A. Schröder, and C. Marques. 2013. Gel-assisted formation of giant unilamellar vesicles. *Biophysical Journal*. 105:154–164. doi:10.1016/j.bpj.2013.05.024.

Wenzel, E.M., S.W. Schultz, K.O. Schink, N.M. Pedersen, V. Nähse, A. Carlson, A. Brech, H. Stenmark, and C. Raiborg. 2018. Concerted ESCRT and clathrin recruitment waves define the timing and morphology of intraluminal vesicle formation. *Nature Communications*. 9. doi:10.1038/s41467-018-05345-8.

Wernert, F., S.B. Moparthi, F. Pelletier, J. Lainé, E. Simons, G. Moulay, F. Rueda, N. Jullien, S. Benkhelifa-Ziyyat, M.-J. Papandréou, C. Leterrier, and S. Vassilopoulos. 2024. The actin-spectrin submembrane scaffold restricts endocytosis along proximal axons. *Science*. 385:eado2032. doi:10.1126/science.ado2032.

Wheeler, S., and D.J. Sillence. 2020. Niemann–Pick type C disease: cellular pathology and pharmacotherapy. *Journal of Neurochemistry*. 153:674–692. doi:10.1111/jnc.14895.

Wilfling, F., M. Kaksonen, and J. Stachowiak. 2023. Protein condensates as flexible platforms for membrane traffic. *Current Opinion in Cell Biology*. 85:102258. doi:10.1016/j.ceb.2023.102258.

Ybe, J.A., F.M. Brodsky, K. Hofmann, K. Lin, S.-H. Liu, L. Chen, T.N. Earnest, R.J. Fletterick, and P.K. Hwang. 1999. Clathrin self-assembly is mediated by a tandemly repeated superhelix. *Nature*. 399:371–375. doi:10.1038/20708.

Yuan, F., H. Alimohamadi, B. Bakka, A.N. Trementozzi, K.J. Day, N.L. Fawzi, P. Rangamani, and J.C. Stachowiak. 2021. Membrane bending by protein phase separation. *Proc. Natl. Acad. Sci. U.S.A.* 118:e2017435118. doi:10.1073/pnas.2017435118.

Zanin, N., C. Viaris de Lesegno, J. Podkalicka, T. Meyer, P. Gonzalez Troncoso, P. Bun, L. Danglot, D. Chmiest, S. Urbé, J. Piehler, C.M. Blouin, and C. Lamaze. 2023. STAM and Hrs interact sequentially with IFN-α Receptor to control spatiotemporal JAK–STAT endosomal activation. *Nat Cell Biol*. 25:425–438. doi:10.1038/s41556-022-01085-6.

Zhao, H., and P. Lappalainen. 2012. A simple guide to biochemical approaches for analyzing protein-lipid interactions. *Mol. Biol. Cell*. 23:2823–2830. doi:10.1091/mbc.E11-07-0645.

Zhao, X., G. Bartolucci, A. Honigmann, F. Jülicher, and C.A. Weber. 2021. Thermodynamics of wetting, prewetting and surface phase transitions with surface binding. *New J. Phys.* 23:123003. doi:10.1088/1367-2630/ac320b.

Figures

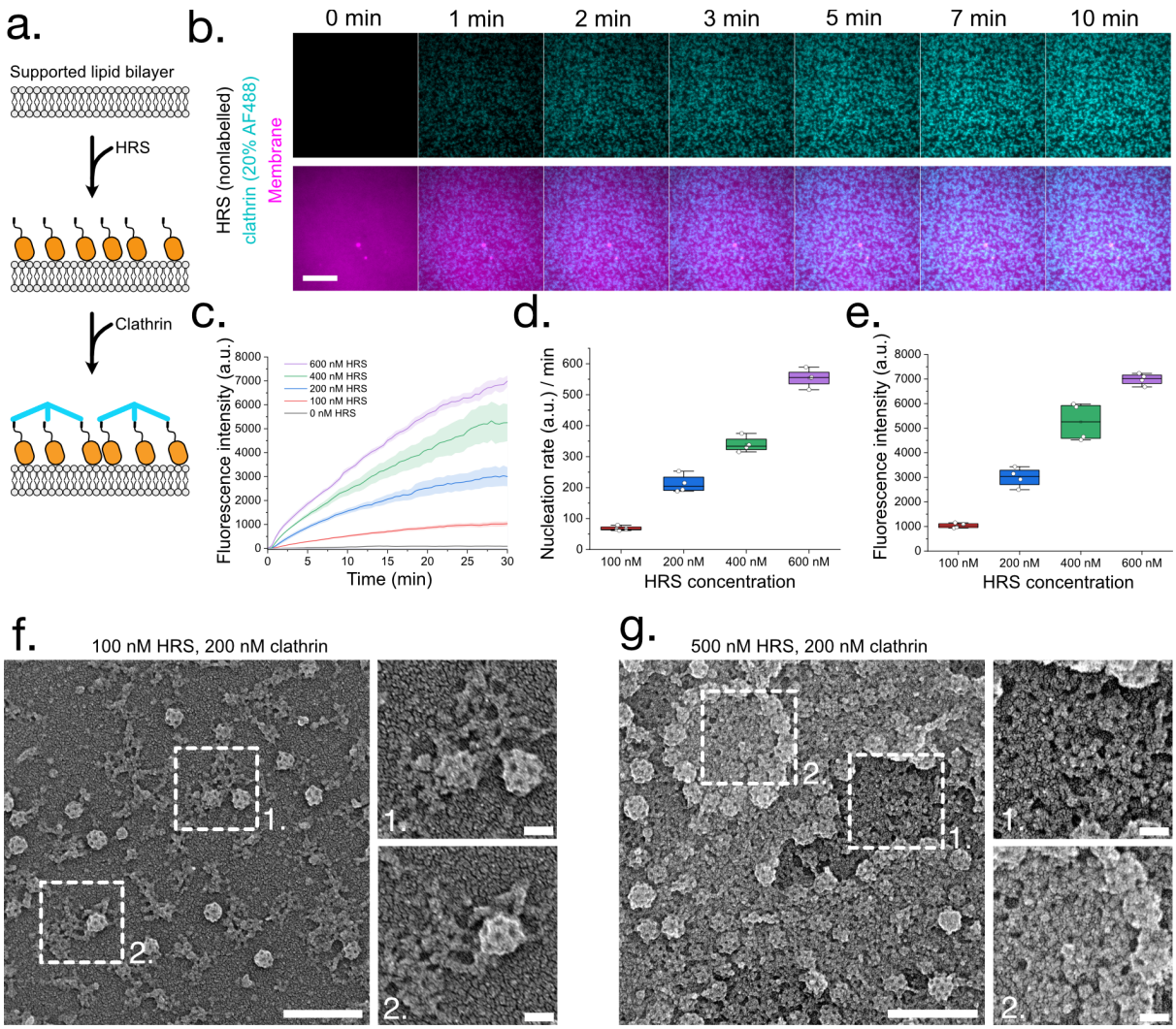

Figure 1. HRS recruits clathrin on membranes as flat patches and spherical cages
a. A schematic illustration of the reconstitution strategy on supported lipid bilayers using sequential protein addition with a microfluidics device. **b.** The recruitment of 200 nM clathrin (20% AlexaFluor-488 labeled) over time on supported lipid bilayers preincubated with 500 nM nonlabelled HRS. The scale bar is 10 µm. N=4 experiments. **c.** The recruitment of 200 nM clathrin (20% AlexaFluor-488 labeled) over time with different HRS concentrations. Data is the mean of four experiments with standard deviations shown. **d-e.** Nucleation rates (**d**) and final clathrin fluorescence intensities (**e**) plotted over HRS concentration from the data in panel b. **f-g.** Representative PREM images of reconstituted HRS-clathrin lattices on supported lipid bilayers imaged with platinum electron microscopy. Scale bars for larger images are 300 nm and for zoom-in images 50 nm. Two different HRS concentrations were used: **f.** 100 nM HRS and **g.** 500 nM HRS with clathrin concentration being 200 nM in both samples.

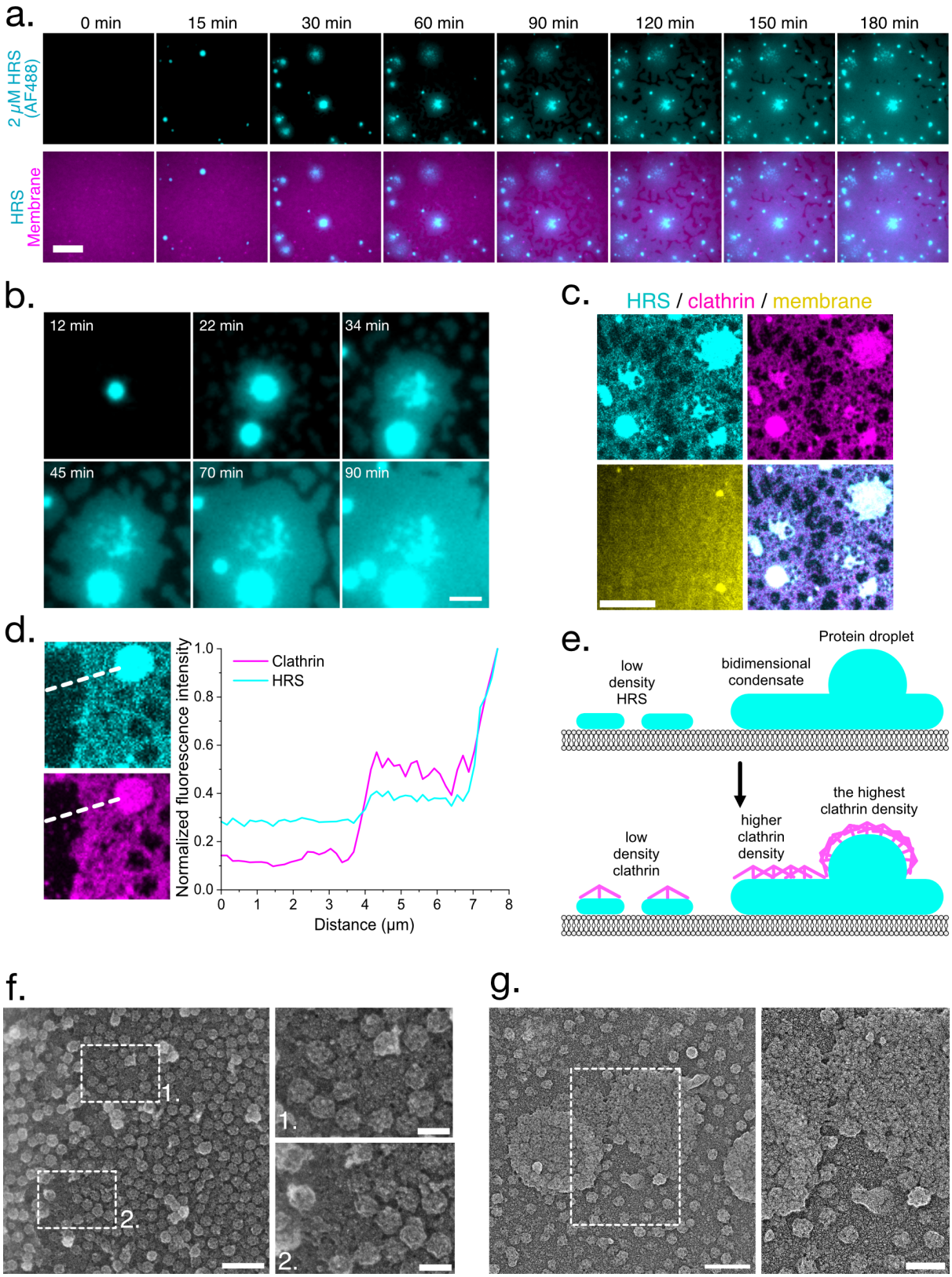

Figure 2. Clathrin assembles on two-dimensional HRS condensates
a. Representative fluorescence timelapse images of 2 μM AlexaFluor-488 labeled HRS on supported lipid bilayer containing. The scale bar is 10 μm. N=4 experiments. **b.** A representative example of HRS condensate droplets spreading on the membrane over time, and droplet getting dispersed. The scale bar is 5 μm. N=4 experiments. **c.** Representative fluorescence microscopy images of 2 μM HRS (AlexaFluor-488 labeled) and 200 nM clathrin (AlexaFluor-568 labeled) on supported lipid bilayers, forming clathrin-coated

bidimensional condensates. The scale bar is 10 μm. **d.** Line profile analysis of AlexaFluor-488 labeled HRS and AlexaFluor-568 labeled clathrin over three HRS populations on supported bilayers. HRS and clathrin fluorescence intensities were normalized to the highest intensity values. **e.** A schematic illustration of three HRS populations: 1) low-density patches, 2) a two-dimensional condensate, 3) Droplet condensate, and how clathrin assembles onto these HRS populations. **f.** Representative platinum replica microscopy images of 2 μM HRS and 200 nM clathrin at room temperature. Scale bars are 300 nm for larger image and 100 nm for zoom-in. **g.** Representative platinum replica microscopy images of 1 μM HRS and 200 nM clathrin with 4°C incubation. Scale bars are 300 nm for larger image and 150 nm for zoom-in.

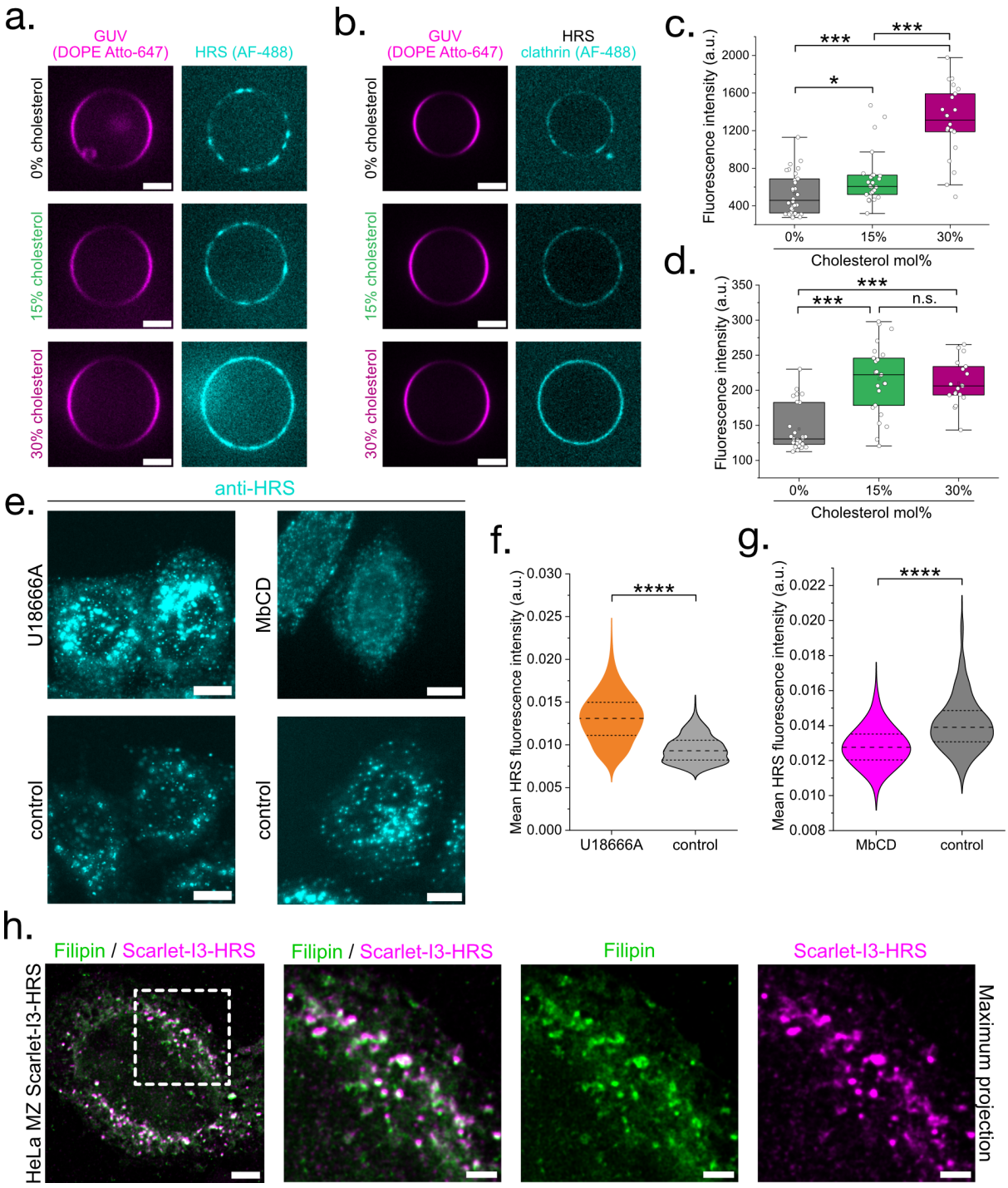

Figure 3. Cholesterol enhances the recruitment of HRS onto the membrane *in vitro* and in cells
a. Representative fluorescence microscopy images of PI3P-rich GUVs with indicated cholesterol concentrations and 500 nM labeled HRS. N=3 experiments. Scale bars are 5 µm. **b.** Representative fluorescence microscopy images of PI3P-rich GUVs with indicated cholesterol concentrations and 500 nM nonlabelled HRS and 200 nM clathrin (20% labeled). N=3 experiments. Scale bars are 5 µm. **c.** The analysis of fluorescence intensity of labeled HRS on GUV membrane (from data in panel a) with different cholesterol concentrations. Each data point represents an individual GUV. The experiment was repeated three times (N=3). **d.** The analysis of fluorescence intensity of labeled clathrin on GUV membrane with different cholesterol concentrations. Each data point represents an individual GUV. The experiment was repeated three times (N=3). **e.** Representative fluorescence microscopy images of HeLa cells treated with U18666A or MβCD, and their corresponding control cells. The scale bar is 10 µm. N=3 experiments. Scale bars are 10 µm. **f.** Mean HRS fluorescence intensity in U18666A treated and control HeLa cells.

Experiments was repeated three times (N=3). **g.** Mean HRS fluorescence intensity in MbCD treated and control HeLa cells. Experiments was repeated three times (N=3). **h.** Representative maximum projection images from confocal fluorescence microscopy stack images of Scarlet-i3-HRS (magenta) CRISPR knock-in cell lines with filipin staining (green). The scale bar is 20 μm for larger images and 2 μm for zoom-in images. The experiment was repeated three times (N=3) with similar results. Statistical testing: Kruskal-Wallis test, n.s. = not statistically significant, * $p < 0.05$, *** $p < 0.001$, **** $p < 0.0001$.

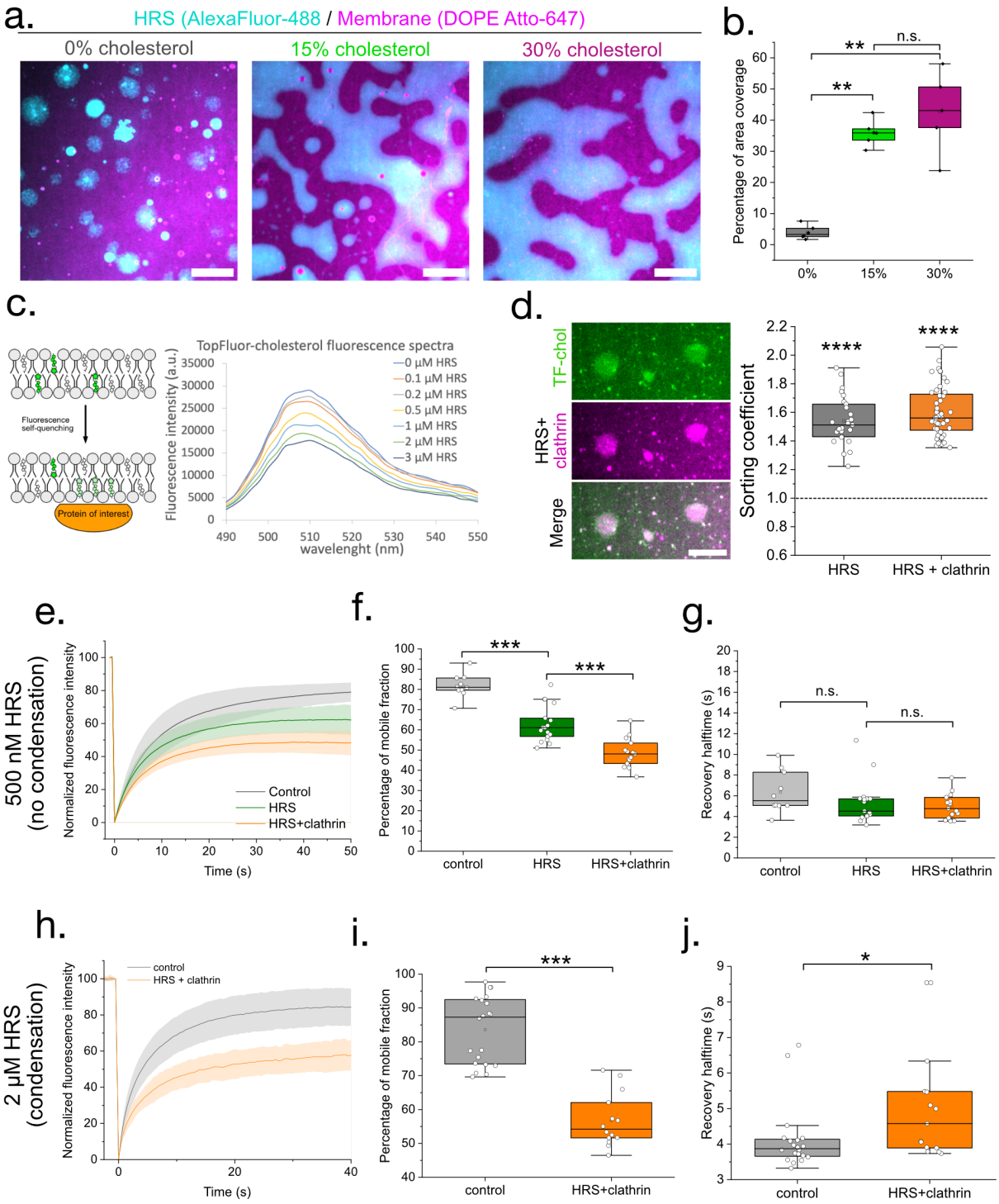

Figure 4. HRS clusters and immobilizes cholesterol

a. Representative fluorescence microscopy images of 2 μM labelled HRS (cyan) on PI3P-rich SLBs (magenta) with varying cholesterol concentrations. N=5 experiments for 0% and 30% cholesterol samples, and N=6 for 15% cholesterol sample. The scale bar is 50 μm. **b.** Percentage labelled HRS covering supported lipid bilayers with different cholesterol concentrations. Each data point represents a mean coverage value in one sample. N=5 experiments for 0% and 30% cholesterol samples, and N=6 for 15% cholesterol sample. **c.** A schematic presentation of fluorescence quenching assay. TopFluor-cholesterol fluorescence spectra with different HRS concentrations. The experiment was repeated three times (N=3) with similar results. **d.** TopFluor-cholesterol sorting coefficient analysis with HRS or HRS and clathrin. A representative fluorescence microscopy images of 1% TopFluor-cholesterol (green) in SLB incubated with 2 μM HRS (unlabeled) and 200 nM clathrin (20% AF-568 labeled, magenta). The scale bar is 5 μm. Sorting

coefficient values were blotted for 2 μM HRS alone and 2 μM HRS + 200 nM clathrin samples. Each data point represents sorting coefficient measurements from independent SLB. The experiment was repeated three times. **e-g.** FRAP experiments to measure TopFluor-cholesterol diffusion in low-density HRS conditions without HRS condensation in control samples (no proteins), with 500 nM HRS, and with 500 nM HRS and 200 nM clathrin. **e.** Recovery curves of TopFluor-cholesterol after photobleaching in control samples (grey) and in the presence of HRS (green), and HRS and clathrin (orange). Dark lines represent mean values and shaded areas standard deviations. **f.** Percentage of mobile fraction of TopFluor-cholesterol FRAP experiment. Each data point represents an independent measurement from in total of three experiments (N=3). **g.** Recovery halftimes of TopFluor-cholesterol FRAP experiments**.** Each data point represents an independent measurement from in total of three experiments (N=3). **h-j.** FRAP experiments to measure TopFluor-cholesterol diffusion under two-dimensional HRS condensates in control samples (no proteins), with 2 μM HRS, and with 2 μM HRS and 200 nM clathrin. **h.** Recovery curves of TopFluor-cholesterol after photobleaching in control samples (grey) and in the presence of HRS and clathrin (orange). Dark lines represent mean values and shaded areas standard deviations. **i.** Percentage of mobile fraction. Each data point represents an independent measurement from in total of three experiments (N=3). **j.** Recovery halftimes of TopFluor-cholesterol in control samples and with 2 μM HRS and 200 nM clathrin. Each data point represents an independent measurement from in total of three experiments (N=3). Statistical testing: Kruskal-Wallis test, n.s. = not statistically significant, * $p < 0.05$, ** $p < 0.01$, *** $p < 0.001$, **** $p < 0.0001$.

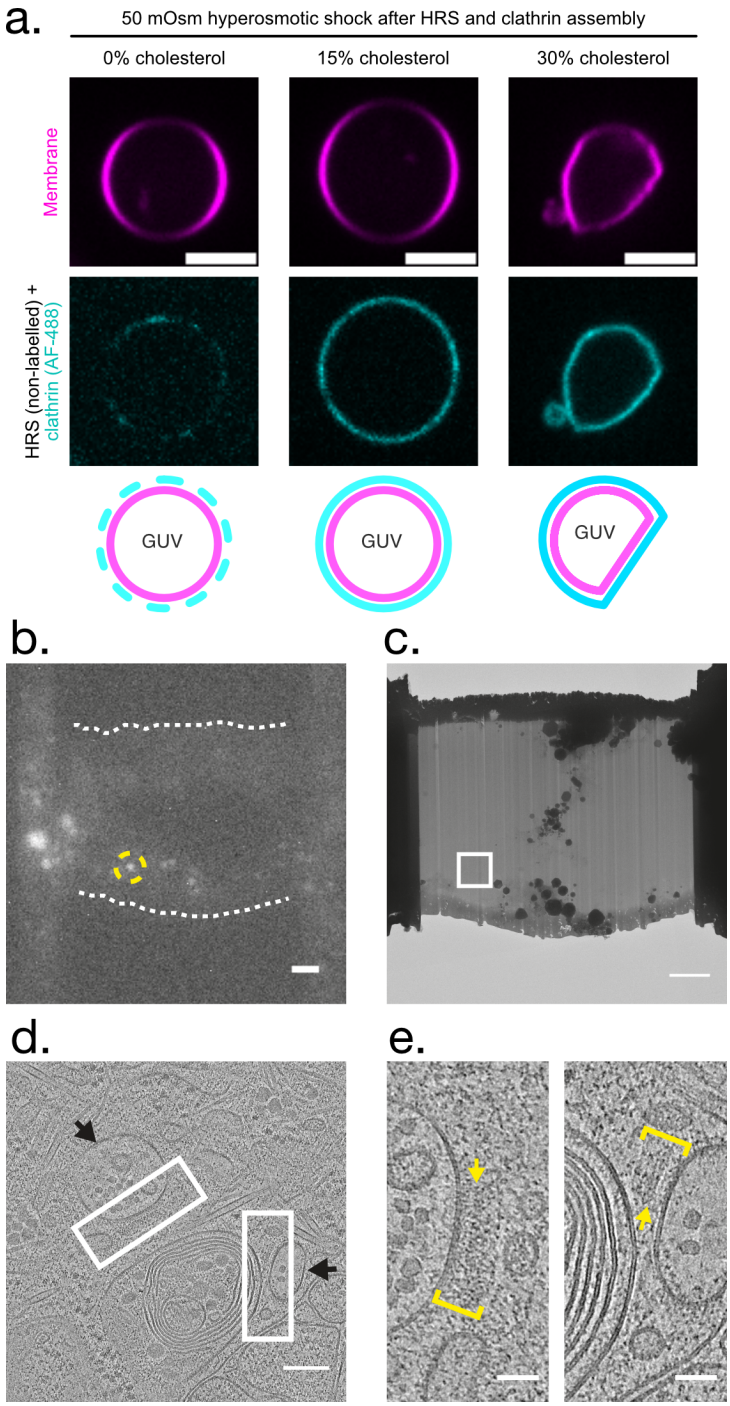

Figure 5. Dense HRS-clathrin lattice promotes flattening of the membrane *in vitro* but not in HeLa cells
a. Representative fluorescence microscopy images of GUVs first incubated with HRS and clathrin and subsequently brought into +50 mOsm osmolarity (hyperosmotic shock). Scale bars are 5 µm. The experiment was repeated three times (N=3) with similar results.
b. A cryo fluorescence microscopy image of a lamella with AlexaFluor-647 EGF signal. Scattered lines indicate the borders of the lamella. The scale bar is 2.5 µm. HeLa cells constitutively expressing HRS mCherry were grown on EM grids, incubated with AlexaFluor-647 labeled EGF cargo, and vitrified upon cargo internalization. Regions of interest were thinned by cryo-FIB milling and the final lamella was imaged by cryo fluorescence microscopy. **c.** A cryo electron microscopy map of lamella. The scale bar is 2.5 µm. **d.** A cryo electron microscopy image of the region indicated by a yellow circle in panel b. Arrows point to multivesicular endosomes. White boxes indicate the regions shown in panel d. The scale bar is 150 nm. **e.** Close-ups corresponding to the white boxes in panel c. Arrows point to multilayered protein densities on endosomal membranes. The scale bar is 50 nm.

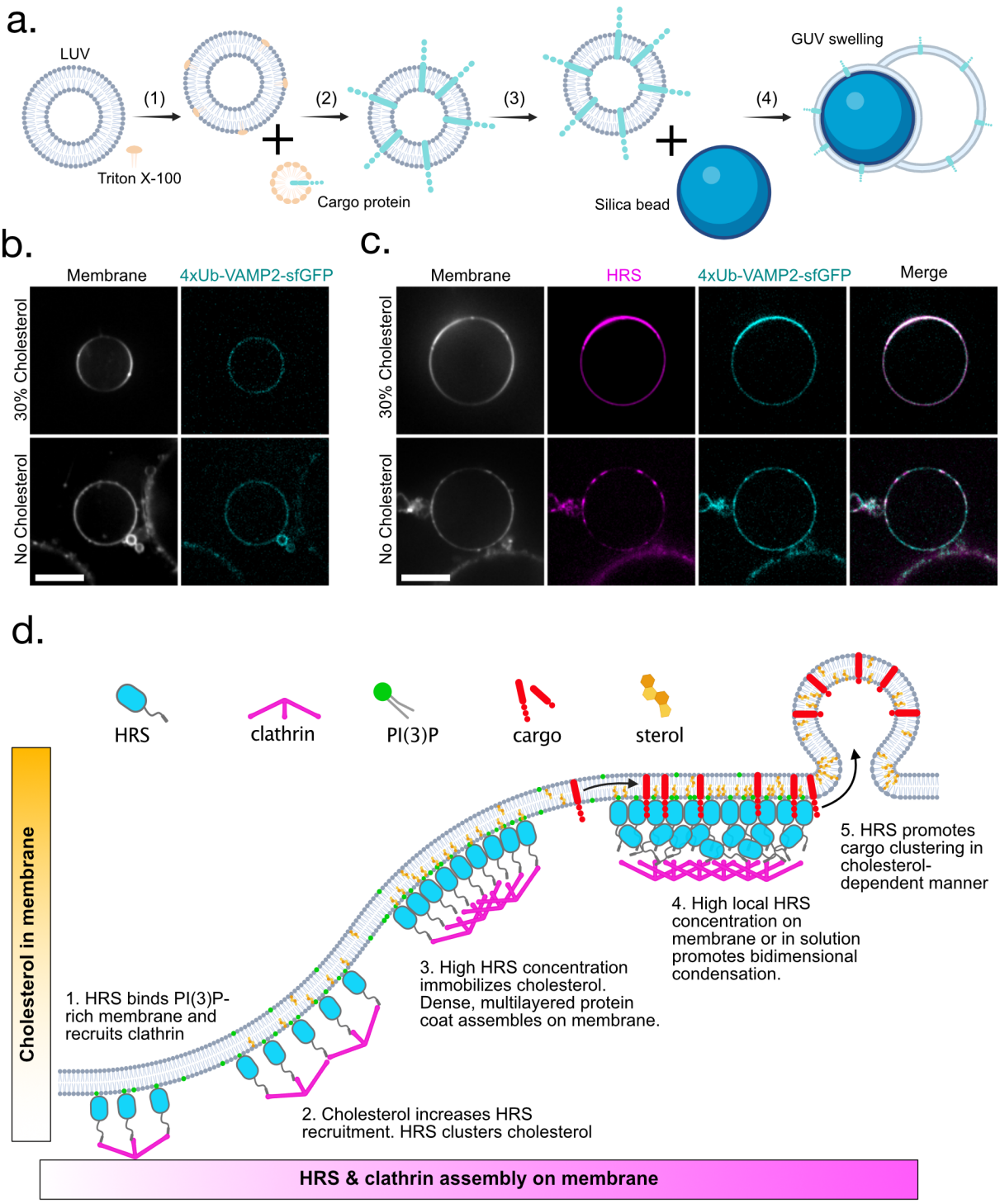

Figure 6. HRS clusters ubiquitylated cargoes in a cholesterol-dependent manner
a. A schematic illustration of reconstitution (see Materials and Methods for details) of 4xubiquitin-VAMP2-sfGFP cargo protein into GUV membrane **b.** Representative fluorescence microscopy images of 4xubiquitin-VAMP2-sfGFP (cyan) reconstituted on GUV membrane (grey) containing either 1% PI(3)P/30% cholesterol or 1% PI(3)P/no cholesterol before the addition of HRS. The scale bar is 5 µm. **c.** Representative fluorescence microscopy images of 4xubiquitin-VAMP2-sfGFP (cyan) reconstituted on GUV membrane (grey) containing either 1% PI(3)P/30% cholesterol or 1% PI(3)P/no cholesterol after addition of 500 nM Scarlet-i3-HRS (magenta). The scale bar is 5 µm. The experiment was repeated four times (N=4) with similar results. **d.** A model of HRS and clathrin assembly on PI(3)P-rich membrane in a cholesterol-dependent manner. HRS binds to PI(3)P through its FYVE domain (1), and clusters cholesterol which leads to increased HRS recruitment on the membrane (2) and finally leads to the formation of a

stable, cholesterol-rich membrane domain under dense HRS clathrin lattice (3). High local protein concentration leads to bidimensional condensation of HRS on the membrane. High-density HRS lattice and stable cholesterol domain under the protein promote cargo sorting under the HRS-clathrin lattice (4). All HRS populations recruit clathrin. Ubiquitinated cargoes get clustered under the HRS-clathrin lattice and cholesterol stabilizes these HRS-cargo clusters (5).